

PL-TR-91-2096

AD-A239 548



2

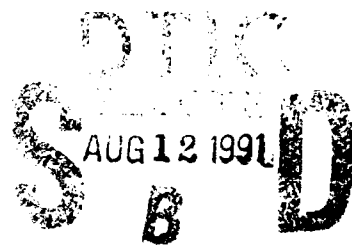
SHOCK PROPAGATION IN CRUSTAL ROCK

Thomas J. Ahrens
Thomas S. Duffy
Allan M. Rubin
Toshimori Sekine

California Institute of Technology
1201 E. California Blvd.
Pasadena, CA 91125

29 April 1991

Final Report
30 September 1988-31 March 1991



APPROVED FOR PUBLIC RELEASE; DISTRIBUTION UNLIMITED



PHILLIPS LABORATORY
AIR FORCE SYSTEMS COMMAND
HANSCOM AIR FORCE BASE, MASSACHUSETTS 01731-5000

91-07392




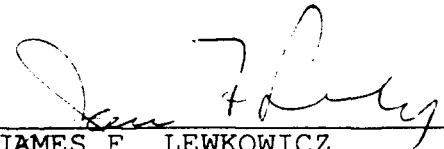
SPONSORED BY
Defense Advanced Research Projects Agency
Nuclear Monitoring Research Office
ARPA ORDER NO. 2309

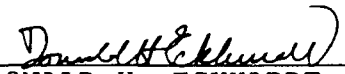
MONITORED BY
Phillips Laboratory
Contract F19628-88-K-0034

The views and conclusions contained in this document are those of the authors and should not be interpreted as representing the official policies, either expressed or implied, of the Defense Advanced Research Projects Agency or the U.S. Government.

This technical report has been reviewed and is approved for publication.


JAMES F. LEWKOWICZ
Contract Manager
Solid Earth Geophysics Branch
Earth Sciences Division


JAMES F. LEWKOWICZ
Branch Chief
Solid Earth Geophysics Branch
Earth Sciences Division


DONALD H. ECKHARDT, Director
Earth Sciences Division

This report has been reviewed by the ESD Public Affairs Office (PA) and is releasable to the National Technical Information Service (NTIS).

Qualified requestors may obtain additional copies from the Defense Technical Information Center. All others should apply to the National Technical Information Service.

If your address has changed, or if you wish to be removed from the mailing list, or if the addressee is no longer employed by your organization, please notify PL/IMA, Hanscom AFB, MA 01731-5000. This will assist us in maintaining a current mailing list.

Do not return copies of this report unless contractual obligations or notices on a specific document requires that it be returned.

REPORT DOCUMENTATION PAGE

1a. REPORT SECURITY CLASSIFICATION UNCLASSIFIED			1b. RESTRICTIVE MARKINGS			
2a. SECURITY CLASSIFICATION AUTHORITY N/A since Unclassified			3. DISTRIBUTION/AVAILABILITY OF REPORT approved for public release; distribution unlimited			
2b. DECLASSIFICATION/DOWNGRADING SCHEDULE N/A since Unclassified						
4. PERFORMING ORGANIZATION REPORT NUMBER(S)			5. MONITORING ORGANIZATION REPORT NUMBER(S) PL-TR-91-2096			
6a. NAME OF PERFORMING ORGANIZATION California Institute of Technology		6b. OFFICE SYMBOL (If applicable)	7a. NAME OF MONITORING ORGANIZATION Phillips Laboratory			
6c. ADDRESS (City, State and ZIP Code) 1201 E. California Blvd. Pasadena, CA 91125			7b. ADDRESS (City, State and ZIP Code) Hanscom AFB, MA 01731-5000			
8a. NAME OF FUNDING/SPONSORING ORGANIZATION		8b. OFFICE SYMBOL (If applicable)	9. PROCUREMENT INSTRUMENT IDENTIFICATION NUMBER F19628-88-K-0034			
8c. ADDRESS (City, State and ZIP Code)			10. SOURCE OF FUNDING NOS.			
11. TITLE (Include Security Classification) SHOCK PROPAGATION IN CRUSTAL ROCK			PROGRAM ELEMENT NO.	PROJECT NO.	TASK NO.	WORK UNIT NO.
			62714E	8A10	DA	AJ
12. PERSONAL AUTHOR(S) Ahrens, Thomas J., Duffy, Thomas S., Rubin, Allan M., Sekine, Toshimori						
13a. TYPE OF REPORT Final		13b. TIME COVERED FROM 880930 TO 910331		14. DATE OF REPORT (Yr., Mo., Day) 1991 April 29		
15. PAGE COUNT 82						
16. SUPPLEMENTARY NOTATION						
17. COSATI CODES			18. SUBJECT TERMS (Continue on reverse if necessary and identify by block number)			
FIELD	GROUP	SUB GR	Granite Hugoniot and Release Data, Equation of State			
19. ABSTRACT (Continue on reverse if necessary and identify by block number)						
<p>New equation of state data for a weathered granite shocked to about 125 GPa are reported and combined with the Westerly granite data of McQueen et al. [1967]. The shock velocity (U_s)-particle velocity (U_p) relations can be fit with two linear regressions: $U_s = 4.70 + 0.46 U_p$ in a range of U_p from 0.7 to about 2 km/sec and $U_s = 2.66 + 1.49 U_p$ in a range of about 2 to 5 km/sec. The third order Birch-Murnaghan equation of state parameters are $K_{os} = 57$ GPa and $K'_{os} = 1.8$ for the low pressure regime and $K_{os} = 304$ GPa and $K'_{os} = 1.2$ for the high-pressure regime.</p> <p>From measurements of partially released states in granite, it is proposed that the high-pressure forms of tectosilicates, including granite, relax isentropically to a metastable, intermediate phase characterized by dense (about 3.7 g/cm^3), highly-disordered, six-fold coordinated phase which is subsequently quenched to diaplectic glasses of density $\sim 2.3\text{ g/cm}^3$, starting at pressure of ~ 10 GPa. We develop an analytical model to describe the release isentropes in the mixed phase regime which prescribe release to a glass phase with increasing transformation to the high pressure phase. Hugoniot and post-shock energies and temperatures derived from the release isentropes are</p>						
20. DISTRIBUTION/AVAILABILITY OF ABSTRACT UNCLASSIFIED UNLIMITED <input type="checkbox"/> SAME AS RPT <input type="checkbox"/> DTIC USERS <input type="checkbox"/>			21. ABSTRACT SECURITY CLASSIFICATION unclassified			
22a. NAME OF RESPONSIBLE INDIVIDUAL James Lewkowicz			22b. TELEPHONE NUMBER (Include Area Code)		22c. OFFICE SYMBOL PI/LWH	

consistent with available data and theoretical expectations for quartz and granite.

Shock wave data for equation of state of muscovite (initial density= 2.835 g/cm^3) was determined up to a pressure of 141 GPa. The shock velocity (U_s) versus particle velocity (U_p) data are fit with a single linear relationship: $U_s = 4.62 (\pm 0.12) + 1.27 (\pm 0.04) U_p$ (km/sec). Third order Birch-Murnaghan equation of state parameters are: $K_{OS} = 52 \pm 4 \text{ GPa}$ and $K'_{OS} = 3.2 \pm 0.3$. The pressure-temperature relation along the Hugoniot suggests that muscovite may dehydrate to KAlSi_3O_8 (hollandite), corundum, and water, with a small volume change, above 80 GPa. Thermodynamic calculations of the equilibrium pressure for the dehydration yields a significantly lower value.

Observed unloading paths from shock pressures up to about 80 GPa are steeper in a density-pressure plane than the Hugoniot, and becomes shallower with increasing shock pressure above that pressure. The changing slope may indicate that devolatilization occurs during unloading above 80 GPa. These equation of state data for muscovite are compared with the previously reported recovery experiments.

TABLE OF CONTENTS

	Page
Conversion Table	
List of Figures	
List of Tables	
Chapter 1 Shock compression and isentropic release of granite	1
Chapter 2 Shock wave equation of state of muscovite	37
List of References	56



Accession For	
NTIS GRA&I	<input checked="" type="checkbox"/>
DTIC TAB	<input type="checkbox"/>
Unannounced	<input type="checkbox"/>
Justification	
By	
Distribution/	
Availability Codes	
Dist	Avail and/or Special
A-1	

LIST OF FIGURES

Figure		Page
1-1	Shock velocity (U_s , km/sec) versus particle velocity (u_p , km/sec) for granite. Solid lines represent linear regressions for the three regimes. Dashed lines represent the calculations for the mineral mixture model with the modal composition, and the dotted line represent the calculation for the oxide mixture model of constituent oxides. These calculations do not suggest any significant difference between the present granite and the Westerly granite [McQueen, 1967]. The elastic velocity obtained for shot #806 (in parentheses) is considered unreliable because of timing uncertainties. HEL = Hugoniot elastic limit.	7
1-2	Pressure-density relation for Hugoniot states of granite. The heavy solid curve corresponds to the Hugoniot equation of state shown in Figure 1. Solid symbols represent the Hugoniot states, and pluses are the measured partial release states (Table 3). Light solid lines in the present study serve only to connect the data sets and are not intended to display the actual release path.	9
1-3	Interface particle velocity profile during shock loading of a weathered granite under dry and wet conditions.	10
1-4	Pressure-volume relations for quartz release paths. Data from Podurets et al. [1976], Chhabildas and Miller [1985], and Swegle [1990]. St = stishovite, MP = mixed phase, Qz = quartz. FQ = fused quartz.	22
1-5	Pressure-volume relations for quartz release paths. Dotted and broken curves illustrate experimental data, and solid curves illustrate Hugoniot curves and calculated release paths. Solid curves are computed based on mixed Hugoniots of Qz and St regimes with mass fractions at 0.1 intervals for St. Below critical pressures (Table 7), the release paths are modeled by straight lines. The zero-pressure volume of post-shock quartz shocked above some 50 GPa was taken to be 0.44 cm ³ /g.	24
1-6	Comparison of pressure-volume relations for measured granite release paths with the model calculations. HP = high-pressure, LP = low pressure, MP = mixed phase, and DG = diaplectic glass.	27

LIST OF FIGURES (Continued)

1-7	Post-shock temperatures for quartz and granite plotted as a function of peak shock pressure. The heavy solid line represents preferred values for post shock temperatures in quartz between 0 and 100 GPa. Post shock temperatures calculated for granite in the mixed phase region are shown as the solid line. Also shown are experimental determinations for SiO ₂ in both the quartz and stishovite stability fields. The data sets of Raikes and Ahrens [1979] and Boslough [1988] are from measurements of post-shock radiation. The data of Chhabildas and Miller [1985] represent calculated values determined from measured wave profiles and the Mie-Gruneisen equation. The dashed line is the calculation of Wackerle for SiO ₂ .	31
1-8	Shock temperatures in SiO ₂ as a function of shock pressure. The heavy solid line represents preferred values of shock temperature in the low pressure, mixed phase, and high pressure regimes of SiO ₂ . The steep P-T slope calculated for the mixed phase region in this study contrasts with the shallow slope calculated by Wackerle [1962]. The data of Lyzenga et al. [1983] were obtained from pyrometer measurements. The present results agree well with the extrapolated trends from this data set.	32
1-9	Shock temperatures in granite as a function of shock pressure. Preferred values of the shock temperature of granite in the low pressure and mixed phase regions are shown by the heavy solid line. In the mixed phase region, granite temperatures are similar to those in SiO ₂ . The temperature at the top of the mixed phase region is ~700 K lower than calculated values for the high pressure phase of granite assuming $\gamma_0 = 1$ and $C_v = 1.19$ J/gmK.	34
2-1	Shock velocity (U _s , km/sec) versus particle velocity (U _p , km/sec) for muscovite. Shock velocity at U _p =0 is within the range of acoustic bulk sound velocity for muscovite [Vaughan, 1986].	42
2-2	Pressure-density relations for Hugoniot state of muscovite. Solid circles are from present study, broken curve is for mineral mixtures, and dotted curve assumes oxide mixture model [Telegin, 1980]. Pluses are for the static compression for muscovite [Bridgman, 1949]. The zero-pressure densities at points 1, 2 and 3 correspond to mixtures of orthoclase + Al ₂ O ₃ +H ₂ O, of wadeite + kyanite + Al ₂ O ₃ +H ₂ O, and KAlSi ₃ O ₈ (hollandite) + Al ₂ O ₃ +H ₂ O, respectively.	43

LIST OF FIGURES (Concluded)

- | | | |
|-----|--|----|
| 2-3 | Pressure-temperature projection of phase boundaries and muscovite Hugoniot. Circles represent the Hugoniot calculation using the heat capacity at 298K and squares represent those using the value at 1000 K. Abbreviations: Hol=hollandite KAlSi_3O_8 , Cor= Al_2O_3 ; Or=orthoclase and Liq=liquid. Solid curve was experimentally determined by Huang and Wyllie [1973]. | 49 |
| 2-4 | Pressure-density relations for muscovite showing adiabatic release states. Solid circles are Hugoniot states and pluses represent measured partial release states (Table 3). Solid lines serve only to connect the data sets and are not intended to represent the actual release path. Arrows indicate calculated slopes obtained from eq. (31). | 52 |

LIST OF TABLES

Chapter 1		Page
1	Chemical Compositions and Model Compositions of Several Granites Used for the Equation of State Experiments	11
2	Equation of State Parameters of Materials Used in the Present Study	12
3	Experimental Results for Granite	13
4	A Comparison of Equation of State for Granites	14
5	A Comparison of VISAR Data With the Impedance Match Calculations for Final Shock State Based on Equation of State for Granite	16
6	Summary of Equation of State Parameters of Granite (Gra), Quartz (Qz), and Feldspar (Fld) for the Low Pressure (LP) and High-Pressure Regime (HP)	20
7	Summary of Equation of State Parameters of Model Release Adiabats for Quartz	25
8	Summary of Equation of State Parameters of Model Release Adiabats for Granite	28
Chapter 2		
1	Chemical Composition (wt %) of Muscovite	39
2	Shock Equation of State Parameters for Flyers, Drivers, and Buffers Used in the Present Study	44
3	Hugoniot and Partial Release States of Muscovite (initial density: $2.835 \pm 0.002 \text{ g/cm}^3$)	53

Conversion factors for U.S. Customary to metric (SI) units of measurement

<div> <div>MULTIPLY</div> <div>→</div> <div>BY</div> </div>		<div> <div>TO GET</div> <div>←</div> <div>BY</div> </div>		<div> <div>→</div> <div>TO GET</div> </div>
<div> <div>TO GET</div> <div>←</div> </div>		<div> <div>BY</div> <div>←</div> </div>		<div> <div>←</div> <div>DIVIDE</div> </div>
angstrom	1.000 000 X E -10			meters (m)
atmosphere (normal)	1.013 25 X E +2			kilo pascal (kPa)
bar	1.000 000 X E +2			kilo pascal (kPa)
barn	1.000 000 X E -28			meter ² (m ²)
British thermal unit (thermochemical)	1.054 350 X E +3			joule (J)
calorie (thermochemical)	4.184 000			joule (J)
cal (thermochemical)/cm ²	4.184 000 X E -2			mega joule/m ² (MJ/m ²)
curie	3.700 000 X E +1			giga becquerel (GBq)
degree (angle)	1.745 329 X E -2			radian (rad)
degree Fahrenheit	$t_F = (t_C + 459.67)/1.8$			degree kelvin (K)
electron volt	1.602 19 X E -19			joule (J)
erg	1.000 000 X E -7			joule (J)
erg/second	1.000 000 X E -7			watt (W)
foot	3.048 000 X E -1			meter (m)
foot-pound-force	1.355 818			joule (J)
gallon (U.S. liquid)	3.785 412 X E -3			meter ³ (m ³)
inch	2.540 000 X E -2			meter (m)
jerk	1.000 000 X E +9			joule (J)
joule/kilogram (J/kg) (radiation dose absorbed)	1.000 000			Gray (Gy)
kilotons	4.183			terajoules
kip (1000 lbf)	4.448 222 X E +3			newton (N)
kip/inch ² (ksi)	6.894 757 X E +3			kilo pascal (kPa)
kip	1.000 000 X E +2			newton-second/m ² (N-s/m ²)
micron	1.000 000 X E -6			meter (m)
mil	2.540 000 X E -5			meter (m)
mile (international)	1.609 344 X E +3			meter (m)
ounce	2.834 952 X E -2			kilogram (kg)
pound-force (lbs avoirdupois)	4.448 222			newton (N)
pound-force inch	1.129 848 X E -1			newton-meter (N-m)
pound-force/inch	1.751 268 X E +2			newton/meter (N/m)
pound-force/foot ²	4.788 026 X E -2			kilo pascal (kPa)
pound-force/inch ² (psi)	6.894 757			kilo pascal (kPa)
pound-mass (lbm avoirdupois)	4.535 924 X E -1			kilogram (kg)
pound-mass-foot ² (moment of inertia)	4.214 011 X E -2			kilogram-meter ² (kg-m ²)
pound-mass/foot ³	1.601 846 X E +1			kilogram/meter ³ (kg/m ³)
rad (radiation dose absorbed)	1.000 000 X E -2			*Gray (Gy)
roentgen	2.579 760 X E -4			coulomb/kilogram (C/kg)
shake	1.000 000 X E -8			second (s)
slug	1.459 390 X E +1			kilogram (kg)
torr (mm Hg, 0° C)	1.333 22 X E -1			kilo pascal (kPa)

*The becquerel (Bq) is the SI unit of radioactivity; 1 Bq = 1 event/s.

**The Gray (Gy) is the SI unit of absorbed radiation.

A more complete listing of conversions may be found in "Metric Practice Guide E 380-74," American Society for Testing and Materials.

CHAPTER 1

**SHOCK COMPRESSION AND ISENTROPIC RELEASE
OF GRANITE**

Toshimori Sekine¹⁾, Allan M. Rubin²⁾, Thomas S. Duffy, and Thomas J. Ahrens

Lindhurst Laboratory of Experimental Geophysics

Seismological Laboratory 252-21

California Institute of Technology

Pasadena, CA 91125, U.S.A.

**1) Permanent Address: National Institute for Research in Inorganic Materials, Tsukuba 305
Japan**

**2) Present Address: Department of Geological Sciences, Brown University, Providence,
RI 02912**

INTRODUCTION

The present report is divided into two chapters. Chapter 1 deals with the equation of state of granite. The analysis of the data for granite utilizes the equation of state of mica (muscovite), which is reported in Chapter 2. Shock Hugoniot data on silicate rocks and minerals all demonstrate major shock-induced phase transformations (e.g. see van Thiel [1977]; Marsh [1980]; Trunin [1986]). The shock response of this class of materials is of importance in describing shock-propagation from impact and explosive sources on the earth and other planetary surfaces as well having application in the study of the Earth's interior.

Granitic rocks are the most common component of the upper continental crust, and consist mainly of quartz and feldspars. The Hugoniots of tectosilicates and rocks composed chiefly of tectosilicates are all quite similar. A number of studies have been performed to measure the high-pressure properties of these minerals and their mixtures (e.g. Wackerle [1962]; Ahrens et al. [1969]; Grady et al. [1975]; Lyzenga et al. [1983]). The derived equation of state parameters have been compared with theoretical considerations (e.g. McQueen et al. [1963]; Ahrens et al. [1969]). The onset of shock-induced phase transformations usually does not occur at the thermodynamic equilibrium pressure or temperature. For example, in the case of quartz, the shock-induced high pressure phase is inferred to be stishovite [McQueen et al., 1963] and this identification is consistent with shock wave recovery experiments (e.g. Milton and DeCarli [1963]). For feldspars, the measured Hugoniots above 30 GPa can be interpreted in terms of a high-pressure polymorph with the hollandite structure [Ahrens et al., 1969; Sekine and Ahrens, 1991].

Shock recovered samples of quartz and feldspars from above 25-30 GPa indicate transformation to diaplectic glasses which are characterized by higher refractive indices and densities than normal fused glasses of the same composition [DeCarli and Jamieson, 1959; Heyman and Hörz, 1990; Kleeman, 1971; Velde et al., 1989; Wackerle, 1962]. These diaplectic glasses have been intensively studied (e.g. Stöffler and Hornemann [1972]). Are

these diaplectic glasses characteristic of tectosilicates? Are they produced during shock compression or during isentropic release? If formation of glass occurs upon isentropic release, what is the phase present in the compressed state and at what pressure does the shocked tectosilicate transform to diaplectic glass?

Recently, isothermal compression of tectosilicates as well as fayalite in the diamond anvil cell at room temperature indicates that transformation to a dense, amorphous phase occurs with an increase in the coordination of silicon and aluminum by oxygen [Hemley et al., 1988; Williams and Jeanloz, 1989; Williams et al., 1990].

The purpose of this study is to present new experimental data for Hugoniot and partially released states of a weathered granite, to synthesize these and previous data, and to generate a complete equation of state. Initially, we summarize available data on the equation of state of granite as well as its major constituents, quartz and feldspar. The release adiabat states are described in terms of the third-order Birch Murnaghan equation of state and compared with those for quartz and feldspars. We then construct analytic expressions for the release isentropes in the low-pressure, mixed-phase, and high-pressure regimes. The mixed phase and high-pressure release isentropes are described in terms of frozen release isentropes [Grady et al., 1974; Swegle, 1990] and upon release to pressures in the 2 to 10 GPa range, the high-pressure phase is assumed to transform to glass as indicated by a number of release data [Ahrens and Rosenberg, 1968; Chhabildas and Grady, 1984; Chhabildas and Miller, 1985; Podurets et al., 1976].

Experimental

The chemical composition of the weathered granite used in the present study was determined by electron microprobe analyses of a glass formed from rock powder quenched in water. The weathered granite was melted at 1600°C in air to obtain a homogeneous glass. Modal analysis of the weathered granite was determined by point counting. Table 2 lists the chemical composition and the mode, together with the compositions of the other

granites for which equations of state have been measured [Chhabildas and Grady, 1984; Marsh, 1980; Van Thiel, 1977]. The chemical composition of all the granites is similar.

The present shock specimens were cut from a disk, 10 cm in diameter and 3 cm thick. Bulk densities ranged between 2.619-2.642 g/cm³, while crystal densities ranged from 2.640-2.645 g/cm³, indicating that porosity of the samples is low. The measured longitudinal and shear sound velocities were 5.36 ± 0.10 and 3.3 ± 0.2 km/sec, respectively.

Shock compression was conducted by launching impactors with the Caltech 25-mm bore two-stage light gas gun and a 40-mm bore propellant gun. Metal flyer plate-bearing projectiles were used to impact the samples. The metal flyer plates were Al or Ta. In each experiment, the impact velocity of the projectile is measured by the flash x-ray method and the shock wave velocity is determined by measuring the travel time of the shock wave through the sample of known thickness by means of a rotating-mirror or an image-converter streak camera. Flat and inclined mirrors were employed to observe the shock wave travel time [Ahrens, 1987]. The Hugoniot state is calculated by applying the impedance match conditions to the measured initial density, impact velocity and shock wave velocity.

A partial or fully released state is also determined by a free-surface or buffer impedance mismatch observation, reduced by way of the Riemann-integral formalism [Lyzenga et al., 1983; Rice et al., 1958]. Lexan and polyethylene were used as buffer materials, mounted at the rear of the sample. Streak camera cut offs could not always be observed for the buffer.

A velocity sensitive interferometer (VISAR) [Barker and Hollenbach, 1972] was employed to investigate compressive wave profiles in dry and water-saturated granite at low stresses (~ 10 GPa). This technique makes use of the Doppler shift of reflected laser light produced by the motion of a diffuse surface. Interference fringes proportional to the velocity of the reflector are developed in a modified Michelson interferometer and recorded

using photo-multiplier tubes (Burle 7764) and digitizing oscilloscopes (HP 54111D). The VISAR used in the present experiments incorporates the push-pull modification [Hemming, 1979] for improved signal quality. The time resolution of our VISAR is estimated to be 5 ns and the velocity resolution limit is about 10 m/s. The target assembly for these experiments consisted of an aluminum driver plate (1.5 mm thick), a granite target (6.25 mm), a diffuse reflecting aluminum buffer (0.75 mm), and a LiF window (8 mm). For one shot (#806), the target was held in an aluminum cup and was water-saturated in vacuum. The shock equations of state for Al, Ta, LiF, lexan and polystyrene employed in these and the Hugoniot experiments are summarized in Table 2. The travel time through the sample and reflector was read from the velocity profile and corrected to calculate the velocities of elastic and plastic waves.

RESULTS

The results of the present experiments are given in Table 3, and are shown in Figs. 1 and 2. For comparison, the Westerly granite data [McQueen et al., 1967] are also plotted in the figures and included in the analysis.

The shock-velocity (U_s) versus particle velocity (U_p) relations shown in Fig. 1 can be characterized by two linear regressions ($U_s = C_0 + S U_p$) $C_0 = 4.70$ km/sec and $S = 0.46$ in a range of $U_p = 0.7$ to 2.1 km/sec and $C_0 = 2.66$ km/sec and $S = 1.49$ in a range of $U_p = 1.8$ to 4.8 km/sec. Moreover, the elastic portion of the Hugoniot can be approximated by a linear relation of $U_s = 5.36 + 0.88 U_p$ ($U_p = 0 \sim 0.6$ km/sec). The effect of water saturation on elastic shock velocity is not resolved by the present experiments. The bulk sound velocity resulting from the measurements of V_p and V_s for dry granite at 1 atm is 3.77 ± 0.55 km/sec which is close to Westerly granite data [Marsh, 1980]. The value of V_p of granite increases under H₂O-saturated conditions [Nur and Simmons, 1969]. It would seem that the presence of water in granite has a critical influence only in the relatively low pressure regime ($P \leq 0.1$ GPa). It appears that the

small amount of water which can be injected in the granite's pores has little effect in the range of the present experiments.

Table 4 summarizes the U_s - U_p relations for various granites. Their compositions are given in Table 1. Despite their chemical variations, the U_s - U_p relations for granites are all similar. C_0 ranges between 2.10 and 2.66 km/sec and S is between 1.49 and 1.63, when U_p ranges from 1.8 to 6 km/sec. Above $U_p = 5$ km/sec, only a few data are available (biotite-chlorite granite and Soviet granite) and Trunin et al. [1988] obtained a linear relation for the Soviet granite (Table 4).

Telegin et al. [1980] have demonstrated good agreement between the observed Hugoniot and the calculated Hugoniot based upon the oxide mixture model. According to this model,

$$C_0 = a_0 + a_1 \rho_0 + \sum_i a_i Z_i \quad (1a)$$

$$S = b_0 + b_1 \rho_0 + \sum_i b_i Z_i \quad (1b)$$

where ρ_0 is the initial density, Z_i is the weight percentage of component oxide i , and a_0 , a_1 , a_i , b_0 , b_1 , and b_i are constants. The constants reported by Telegin et al. [1980] were used in the present calculations. The calculations are restricted to the high pressure phase region. The results shown in Fig 1 (dotted curve) ($U_s = 2.369 + 1.59 U_p$ km/sec) demonstrate a good approximation to the Hugoniot data in the high pressure regime.

We also apply a mineral mixture model [Al'tshuler and Sharipdzhanov, 1971] to obtain a theoretical Hugoniot for the present weathered granite. In this model,

$$V(P) = \sum_i V_i(P) M_i \quad (2)$$

where V_i is the volume of constituent mineral i at pressure P and M_i is a mass fraction of mineral i . Using the Rankine-Hugoniot equations, U_s and U_p are computed from the

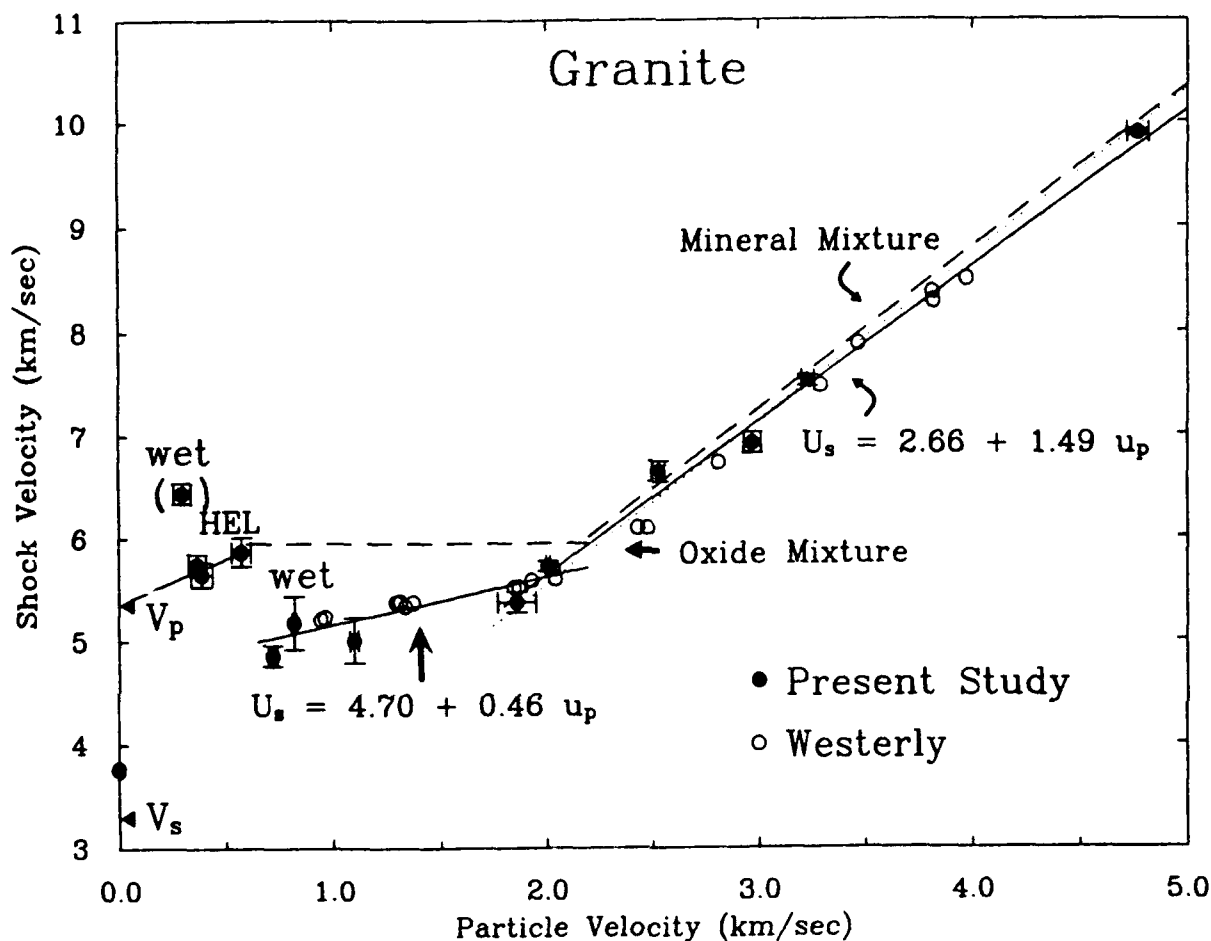


Figure 1-1 Shock velocity (U_s , km/sec) versus particle velocity (u_p , km/sec) for granite. Solid lines represent linear regressions for the three regimes. Dashed lines represent the calculations for the mineral mixture model with the modal composition, and the dotted line represent the calculation for the oxide mixture model of constituent oxides. These calculations do not suggest any significant difference between the present granite and the Westerly granite [McQueen et al., 1967]. The elastic velocity obtained for shot #806 (in parentheses) is considered unreliable because of timing uncertainties. HEL = Hugoniot elastic limit.

resulting P-V relation. The granite is taken to be a mineral mixture consisting of the modal composition (Table 1). The Hugoniot for plagioclase and K-feldspar have been recognized to be insensitive to composition and the microcline Hugoniot [Ahrens et al., 1969; Simakov et al., 1974] was used in the present calculation. The quartz Hugoniot was taken from the data of Wackerle [1962] and Trunin et al. [1970]. The muscovite Hugoniot, which has been recently determined [Sekine et al., 1991a], was also employed to obtain the calculation of the weathered granite Hugoniot. The resulting U_s - U_p relation is shown in Fig. 1 (dashed line). It approximates the experimental data only in the high-pressure regime ($U_p \geq 2.0$ km/sec), but not in the low pressure regime ($U_p < 2$ km/sec).

In Fig. 2, pressure-density relations are plotted for the present granite and Westerly granite. The pressure-density relation may essentially be divided into three parts: low-pressure regime, mixed phase regime and high-pressure regime. The separation between the low-pressure and mixed phase regimes is not complete as in the pressure-density Hugoniot for quartz [Swegle, 1990].

The goal of the VISAR experiments was to determine the effect of water-saturation on the HEL and shock structure in the double shock-wave regime. Impact conditions are listed in Table 3 and particle velocity profiles for the aluminum-LiF interface are shown in Figure 3. In all experiments, two wave structure is visible, but it is less well defined in the case of the wet experiment. The shock velocities for the elastic and plastic waves were estimated from the VISAR profile and thickness of sample by assuming that the elastic and plastic wave velocities of Al-2024 are constant at 6.36 km/sec [Marsh, 1980] and given by the U_s - U_p relations shown in Table 2, respectively. The particle velocity in the Al driver plate is approximated by taking 0.5 of the impact velocity and that in the reflector Al is read from the VISAR record. The calculated results are listed in Table 3. The U_s - U_p relations, which are included in Fig. 1, show good agreement with the Westerly granite data but a considerable divergence from the calculations based on the mineral mixture model. This may indicate the importance of material strength in the low pressure region.

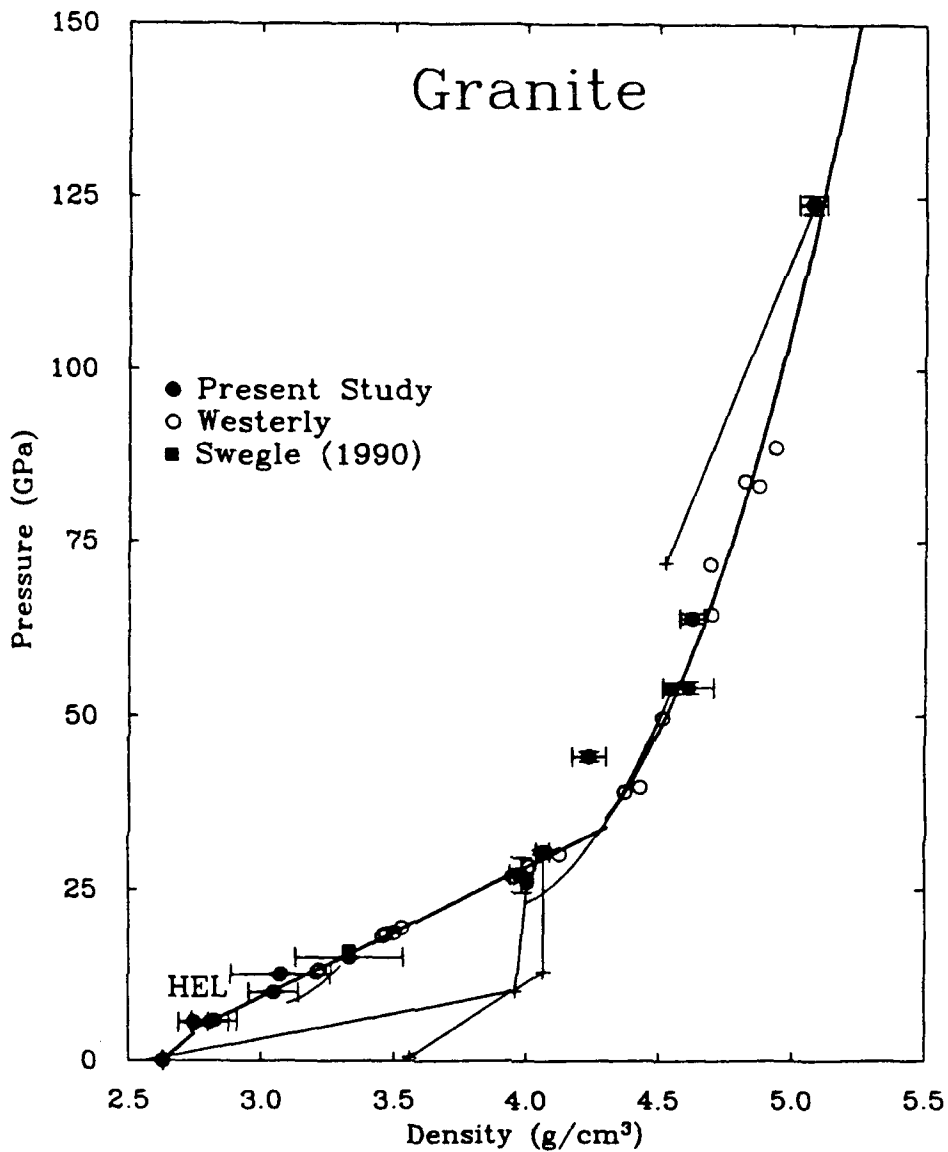


Figure 1-2 Pressure-density relation for Hugoniot states of granite. The heavy solid curve corresponds to the Hugoniot equation of state shown in Figure 1. Solid symbols represent the Hugoniot states, and pluses are the measured partial release states (Table 3). Light solid lines in the present study serve only to connect the data sets and are not intended to display the actual release path.

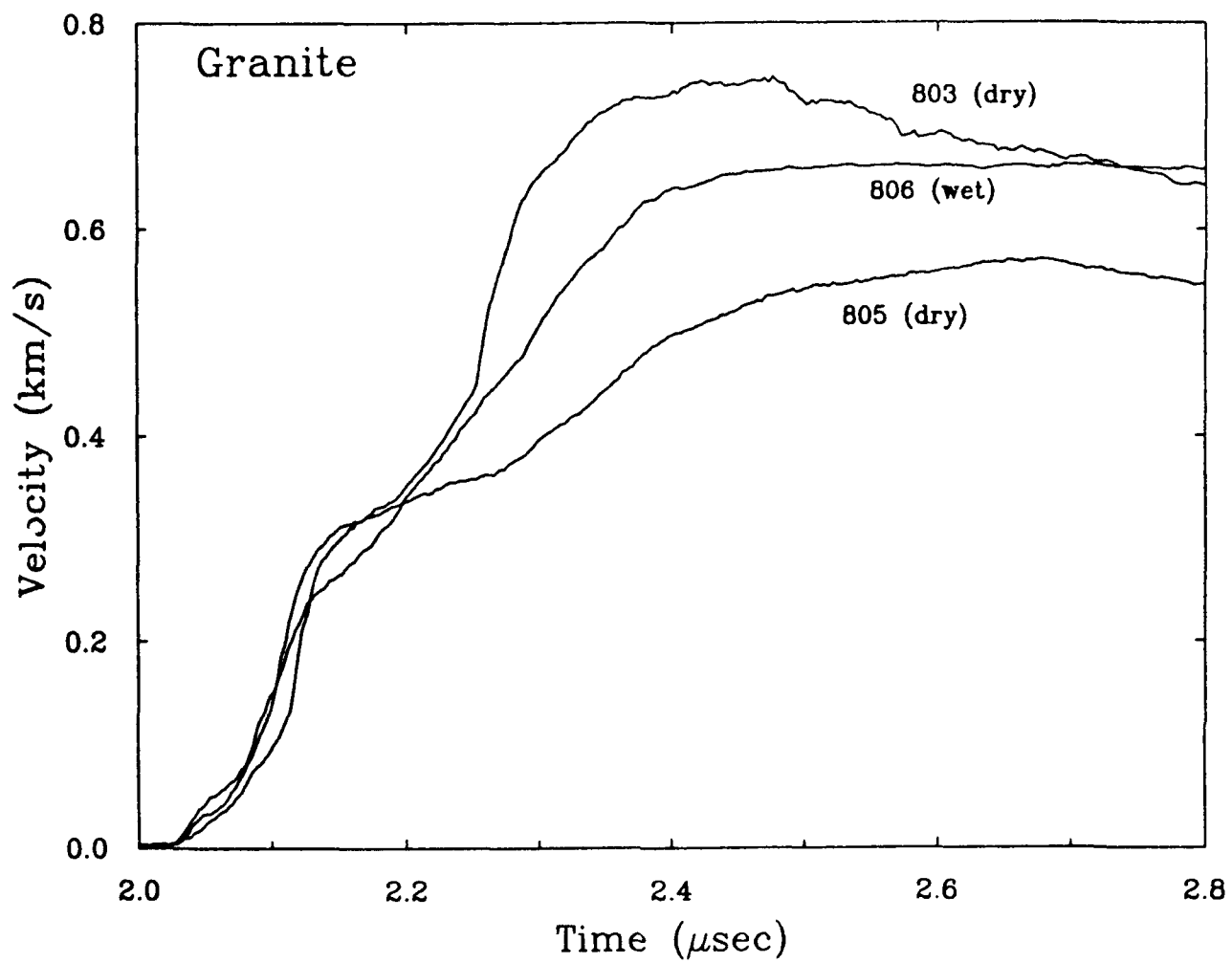


Figure 1-3 Interface particle velocity profile during shock loading of a weathered granite under dry and wet conditions.

Table 1. Chemical Compositions and Modal Compositions of Several Granites
Used for the Equation of State Experiments

	Composition		Mineral Content			
	Present Study(1)	Grey Granite(2)	1	2	3	4
SiO ₂	73.1	71.94	41.3	19.5	28.5	21.1
TiO ₂	0.15	0.26	24.8	26.5	32.5	46.7
Al ₂ O ₃	13.9	13.68	25.3	47.0	35.4	20.3
FeO*	1.09	4.25	8.6	5.0	3.6	4.9
MgO	0.37	0.63	--	~2.5	--	7.0
CaO	0.80	2.96				
MnO	0.02	-----				
K ₂ O	3.93	1.44				
Na ₂ O	4.68	2.94				
H ₂ O	--	1.38				
Total	98.1	99.48				

1. Weathered granite used in the present study.
2. Grey granite from the Nevada Test Site #15 [van Thiel, 1977]
3. Westerly granite [McQueen et al. 1967, Marsh 1980]
4. Biotite-chlorite granite [van Thiel, 1977]

Table 2. Equation of State Parameters of Materials Used in the Present Study

Material	Initial Density (g/cm ³)	U _s =C ₀ +S U _p (km/sec)		
		C ₀ (km/sec)	S	Ref.
Al 2024	2.785	5.328	1.338	1
Ta	16.656	3.43	1.19	2
LiF	2.638	5.15	1.35	1
Lexan	1.193	2.449	1.498	1
Polystyrene foam	6.055	0.243	1.118	1

Ref.

1. Marsh [1980]
2. Mitchell and Nellis [1981]

Table 3. Experimental Results for Granite

Shot #1	Flyer/Driver	Impact Velocity (km/sec)	Hugoniot State				Partial Release State				
			Initial Density (g/cm ³)	Shock Velocity (km/sec)	Particle Velocity (km/sec)	Pressure (GPa)	Density (g/cm ³)	Shock Velocity (km/sec)	Particle Velocity (km/sec)	Pressure (GPa)	Density (g/cm ³)
805	A1	1.21 ±0.01	2.630 ±0.002	elastic	0.39 ±0.05	5.8 ±0.35	2.825 ±0.085				
				plastic 4.86 ±0.10	0.72 ±0.02	10.0 ±0.2	3.050 ±0.093				
806	A1	1.43 ±0.01	2.619 ±0.002	elastic	0.30 ±0.04	5.6 ±0.3	2.747 ±0.055				
				plastic 5.18 ±0.26	0.82 ±0.01	12.6 ±0.3	3.075 ±0.188				
803	A1	1.78 ±0.01	2.628 ±0.002	elastic	0.37 ±0.04	5.6 ±0.3	2.809 ±0.070				
				plastic 5.01 ±0.22	1.10 ±0.02	15.1 ±0.3	3.333 ±0.203				
832	A1	2.21 ±0.01	2.633 ±0.001	elastic	0.575 0.045	8.9 ±1.6	2.919 ±0.102				
				plastic 5.38 ±0.10	1.86 ±0.09	27.1 ±2.5	3.985 ±0.218	lexan 5.00 ±0.12 postshock ---	1.78 ±0.08	10.2 ±0.7	3.960 ±0.046
827	Ta	2.465 ±0.010	2.642 ±0.002	plastic 5.73 ±0.05	2.01 ±0.01	30.4 ±0.3	4.066 ±0.024	lexan 5.45 ±0.06	2.00 ±0.04	13.0 ±0.4	4.065 ±0.118
222	A1	4.54 ±0.005	2.624 ±0.002	plastic 6.64 ±0.10	2.53 ±0.03	44.1 ±0.7	4.238 ±0.063				
229	A1	5.31 ±0.05	2.638 ±0.002	plastic 6.92 ±0.10	2.97 ±0.04	54.1 ±0.9	4.608 ±0.096				
230	Ta	4.09 ±0.04	2.638 ±0.002	plastic 7.52 ±0.05	3.23 ±0.03	64.0 ±0.7	4.621 ±0.045				
220	Ta	6.22 ±0.06	2.625 ±0.002	plastic 9.89 ±0.03	4.77 ±0.05	124.0 ±1.3	5.075 ±0.052	lexan 10.22 ±0.052	5.91 ±0.10	72.0 ±0.08	4.512 ±0.127

Table 4. A Comparison of Equations of State for Granites

No.	Co (km/s)	S	Initial Density (g/cm ³)	U _p Range (km/s)	V _p (km/s)	V _s (km/s)
1	4.70	0.46	2.630	0.7-2.1	5.36±0.10	3.3±0.2
	2.66	1.49		1.8-4.8		
2	2.52	1.50	2.67	2-4	5.64	3.53
3	2.10	1.63	2.62	2.1-4	5.36±0.10	3.3±0.2
	2.59	1.51	2.62	1.8-4		
4	2.22	1.63	2.68	3-6		
5	2.435	1.525	2.60	2.16-5.10		
	3.75	1.28	2.60	5.10-8.9		

Granites Nos. 1 to 4 correspond to the number in Table 1.

Granite No. 5 is from Trunin et al. [1988].

The HEL (Hugoniot elastic limit) has been determined from the VISAR records and the inclined mirror method. The latter indicated a higher value of U_p and a higher pressure for the HEL (Table 3). This may be due to the fact the the HEL pressure increases slightly with increasing driving shock pressure [Ahrens et al., 1969]. The HEL wave velocity demonstrates some scatter for the three shots fired.

In Table 5, the final shock Hugoniot states of granite and the Al reflector are summarized and compared with the measured particle velocity of the reflector at the interface of the LiF window. In this calculation, the Hugoniot for granite was assumed to be a simple linear relation ($U_s = 3.77 + 1.52 U_p$) connecting the two points of the lowest deformational shock state and the bulk sound velocity at 1 atm in the U_s - U_p plot. As seen in Table 5, the difference in the calculated and measured results is very small for shots #805 and #806. For shot #803, a slight optical misalignment resulted in non-normal incidence of the laser beam, in which case the apparent measured velocity is less than the actual particle velocity.

In Figure 3, both the elastic and plastic portions of the wavefront are characterized by long rise times, probably related to the large grain size of the samples. Water-saturation results in a further increase in rise time and obscures the inflection point between the elastic and plastic portions of the wave. According to Figure 3, the amplitude of the plastic precursor is about 20% lower in the case of the wet shot. The lower compressive strength of the wet sample could be due to the presence of water along cracks reducing the effective normal stress and therefore the frictional strength of the flaws, thus promoting brittle failure.

The measured release states of the present granite are shown in Fig. 2, together with the data by Swegle [1990]. The release of shocked granite from about 26-30 GPa Hugoniot pressures was found to occur along pressure-density paths characteristic of the high-pressure phase(s) and at low pressures, final unloading states were close to the low pressure phase initial density. Swegle [1989] also observed that the unloading data of

Table 5. A Comparison of VISAR Data With the Impedance Match
Calculations for Final Shock State
Based on Equation of State For Granite

		$U_s = 3.77 + 1.52 U_p$ km/s		
		U_s	U_p	P
		(km/sec)	(km/sec)	(GPa)
#805	Granite, Hugoniot	4.818	0.689	8.7
	Reflected from Al	4.958	0.782	10.2
	Al, Hugoniot	6.127	0.597	10.2
	Reflected from LiF	6.098	0.576	9.8
	Measured (Al-LiF interface)	----	0.570 (peak)	----
#806	Granite, Hugoniot	5.002	0.811	10.6
	Reflected from LiF	5.159	0.914	12.4
	Al, Hugoniot	6.274	0.707	12.4
	Reflected from LiF	6.240	0.682	11.9
	Measured (Al-LiF interface)	----	0.661 (peak)	----
#803	Granite, Hugoniot	5.288	0.998	13.9
	Reflected from Al	5.464	1.114	16.0
	Al, Hugoniot	6.509	0.883	16.0
	Reflected from LiF	6.469	0.853	15.4
	Measured (Al-LiF interface)	----	0.746 (peak)	---

Note: The upper row of granite corresponds to the interface between driver plate and granite, and the lower one corresponds to that between granite and Al reflector. The upper row of Al corresponds to the interface between granite and Al and the lower responds to that between Al reflector and LiF window.

granite from 27 GPa demonstrated initial unloading characteristic of the high pressure phase. Swegle's [1990] data indicate that the reverse transition is not initiated immediately upon unloading. This behavior can be seen at least up to the Hugoniot pressure of 54 GPa for granite [Swegle, 1990]. However, the release path observed from one datum at the Hugoniot pressure of 124 GPa indicates a shallower slope than the Hugoniot. Swegle [1989] provides a similar unloading profile for granite at 92 GPa. There are several other data which indicate that the release path slope can decrease with increasing shock pressure in the pressure-density plot (Swegle [1990], for rhyolite).

DISCUSSION

The shock wave data are used to obtain equation of state parameters K_{0s} (the zero-pressure adiabatic bulk modulus) and K'_{0s} (its first pressure derivative) for the third order Eulerian finite strain (Birch-Murnaghan) equation of state for granite. We use the approach of Ahrens and Jeanloz [1987]; Jeanloz [1989]; Heinz and Jeanloz [1984] to analyze the Hugoniot data.

The Eulerian strain f is expressed as

$$f = \frac{1}{2} \left[\left(\frac{V_0}{V} \right)^{\frac{2}{3}} - 1 \right] \quad (3)$$

where V and V_0 are Hugoniot and ambient volumes of the sample respectively. The normalized pressure F_{HS} is given by

$$F_{HS} = F_{HS} + \Delta F_{tr} = K_{\alpha}(1 - 2\xi_* f_{3H} + \dots) \quad (4)$$

$$F_{HS} = \frac{1 - \frac{\gamma}{2}[(1 + 2f)^{3/2} - 1]}{3f(1 + 2f)^{3/2}[1 + (2 - 1.5\gamma)f]} P_H \quad (5)$$

$$\Delta F_{tr} = \frac{\rho_o \gamma E_{tr}}{3f[1 + (2 - 1.5\gamma)f]} \quad (6)$$

$$f_{3H} = \frac{f[1 + (2 - \gamma)f]}{1 + (2 - 1.5\gamma)f} \quad (7)$$

and

$$\xi_* = 3(4 - K'_{\alpha}) / 4 \quad (8)$$

where γ is the Gruneisen parameter and P_H is Hugoniot pressure.

The parameters F_{HS} , f_{3H} , and ΔF_{tr} are obtained from the experimental data, and the parameter K_{α} and K'_{α} are obtained from a linear fit to equation 4. γ is calculated according to the following equations

$$\gamma = \gamma_o \left(\frac{V}{V_o} \right)^q \quad (9)$$

and

$$\gamma_o = \frac{\alpha K_{\alpha}}{\rho_o C_p} \quad (10)$$

where α is the volume coefficient of thermal expansion and C_p is the specific heat at constant pressure.

Errors in F_{HS} and f_{3H} are estimated by standard error propagation techniques using the expressions in Ahrens and Jeanloz [1987].

Low Pressure Regime

For granite in the low pressure regime ($P < 20$ GPa), $E_{tr} = 0$, $\rho_o = 2.63$ g/cm³, $\gamma_o = 1.0 \pm 0.5$, and $q = 1.0 \pm 1.0$ were used in the present computation. These values cover

reasonable ranges for γ_0 and q , and the resulting K_{OS} and K'_{OS} are insensitive to the values of γ_0 and q used. An unweighted linear least squares fit to the experimental data below a shock pressure of 20 GPa including the Westerly data yields $K_{OS} = 57$ GPa and $K'_{OS} = 1.8$. A Zero-order fit ($K'_{OS} = 4$) of the experimental data yields $K_{OS} = 40$ GPa. Ultrasonic determinations of K_{OS} give 37 GPa which is close to K_{OS} of quartz.

The bulk moduli for end-member feldspars range between 67 and 106 GPa [Angel et al., 1988]. The value of $K_{OS} = 57$ GPa for granite is consistent with a mixture of quartz and feldspars. The equations of state are summarized in Table 6.

High Pressure Regime

Equation of state parameters are calculated for granite in the high-pressure regime ($P > 39$ GPa) in the same manner as for the low pressure regime. The values of γ_0 and q are not well constrained, however. E_{tr} is estimated to be 0.8 ± 0.5 kJ/g based on the transition energies of quartz to stishovite and feldspars to the hollandite structures.

Although the transition energy varies with feldspar composition, the stated error range for E_{tr} covers the whole range of variation of feldspar composition. The zero-pressure density of the granite in the high pressure regime is calculated to be 4.02 g/cm^3 from stishovite and hollandite densities. The hollandite density varies also with the initial feldspar composition and was approximated by the modal composition. We assumed that $\gamma_0 = 1.0 \pm 0.5$ and $q = 1.0 \pm 1.0$. With these parameters, we obtained an adiabatic bulk modulus of $K_{OS} = 304$ GPa and its first pressure derivative $K'_{OS} = 1.2$. These values are similar to estimates for stishovite based on quartz Hugoniot data [Tan and Ahrens, 1990], although the zero-pressure density differs slightly (by 5%). The datum of shot #222 indicated a larger normalized F_{HS} with 4 times greater error than the others. Swegle [1990] gave the same equation of state parameters for quartz and granite in both the low-pressure and high-pressure regimes. They are compared in Table 6. Recent analyses of Hugoniot data for various feldspars provide ranges of K_{OS} and K'_{OS} as well as the zero-pressure densities,

Table 6. Summary of Equation of State Parameters of Granite (Gra), Quartz (Qz), and Feldspar (Fld) for the Low Pressure Regime (LP) and High-Pressure Regime (HP)

	Gra			Qz 2)			Fld 3)		
	LP	HP		LP	HP		LP	HP	
ρ_0 (g/cm ³)	2.63	4.02 1)		2.65	4.19		2.65	4.287	3.75
K_{os} (GPa)	57	304		37.7	350		37.7	350	200
K_{os}	1.8	1.2		6.4	3.3		6.4	3.3	2.3
E_{tr} (kJ/g)	----	0.8		----	0.89		----	----	0.5
Ref.	1	2		3			2	4	5

1) Obtained as a mixture of 50% stishovite and 50% high-pressure feldspar with the hollandite structure.

2) Quartz transforms to stishovite.

3) Feldspar transforms to the hollandite form.

Ref. 1=Present Study, 2=Swegle [1990], 3=Tan and Ahrens [1990], 4=Angel et al. [1988], and 5=Sekine and Ahrens [1991].

based on shocked feldspars possessing the hollandite structure [Sekine and Ahrens, 1991]. The equation of state parameters for granite are between those of quartz and feldspars for both the low and high pressure regimes.

Release States

The Hugoniot and equation of state parameters for quartz, feldspars and granite are quite similar as summarized in Table 6. The release adiabat states measured for shocked quartz [Chhabildas and Miller, 1985; Podurets et al., 1976], feldspars [Ahrens et al., 1969; Grady and Murri, 1976] and granite [Sekine et al., 1991b; Swegle, 1989; Swegle, 1990] also show similar release paths, depending mainly upon the initial shock state. These release adiabats have been measured by independent methods: impedance mismatch buffer method [Ahrens et al., 1969; Podurets et al., 1976; Sekine et al., 1991b], manganin transducer record [Grady and Murri, 1976] and velocity interferometer (VISAR) [Chhabildas and Miller, 1985; Swegle, 1989].

Quartz has been studied widely under dynamic conditions. Figure 4 shows the release adiabats measured for quartz. The release adiabats from shocked quartz in the mixed phase regime are approximated by unloading paths in which the quantity of low and high pressure phase in the mixture is frozen down to about 8 GPa [Grady et al., 1974; Swegle, 1989]. At this point, the volumes expand to the initial volume with further decreasing pressure.

The release adiabats from the stishovite regime, however, seem to occur along paths leading to less dense zero-pressure material than the zero-pressure density of the high-pressure form (stishovite), especially when the release pressure reaches within the mixed phase regime. It appears that a material with density of about 3.7 g/cm^3 is produced during the unloading process and may then revert to a diaplectic glass on further pressure release to ambient pressure and temperature as observed in the shock-recovery experiments on quartz. This apparent density, in fact, may be a diaplectic glass with six-fold

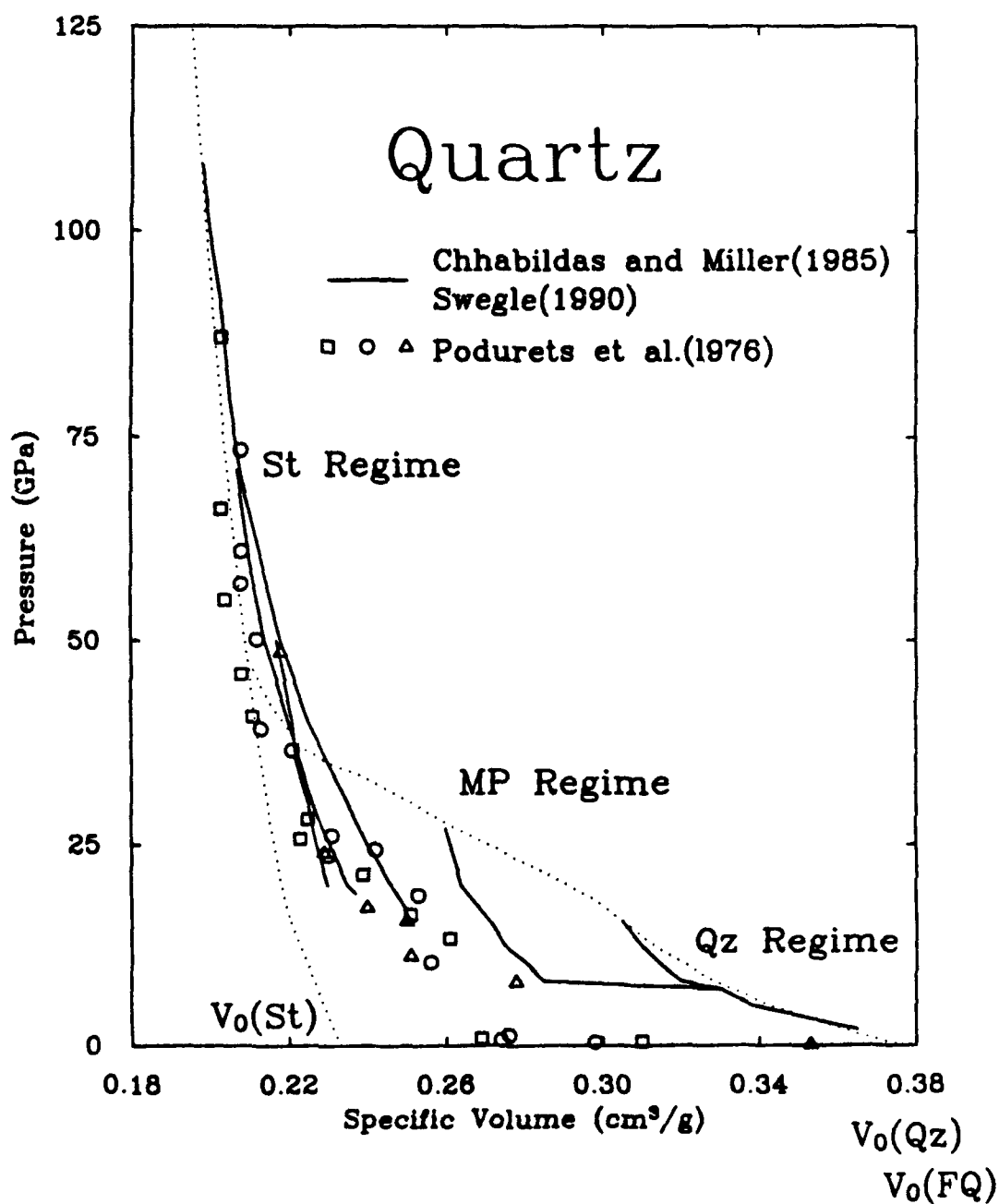


Figure 1-4 Pressure-volume relations for quartz release paths. Data from Podurets et al. [1976], Chhabildas and Miller [1985], and Swegle [1990]. St = stishovite, MP = mixed phase, Qz = quartz. FQ = fused quartz.

coordinated silicon with oxygen . We set the post-shock quartz density to be 2.27 g/cm^3 [Stöffler and Hornemann, 1972]. It is interesting to note that the density ratio of this proposed material to stishovite is close to that of the fused silica glass to quartz. In this context, Chhabildas and Miller [1985] suggest that this material might represent a high density quartz liquid produced above the melting point during unloading.

Figure 5 displays calculations of release adiabats in the mixed phase regime based on the mixing of two Hugoniot for the quartz regime and the stishovite regime in a range of pressure for the mixed phase regime. In this model, the mass fraction of stishovite is frozen in the mixed phase during the release state until the pressure drops down to a critical value represented by the relation $P \text{ (GPa)} = 32.2 - 85.5 V \text{ (cm}^3\text{/g)}$ shown in Fig. 5. Further release causes the formation of diaplectic glass and the final volume of post-shock quartz is given by the relation $V \text{ (cm}^3\text{/g)} = 0.063M + 0.377$ at ambient conditions, where M is the mass fraction of stishovite at the Hugoniot state, as listed in Table 7. This model calculation is compared with the experimental data [Chhabildas and Miller, 1985; Podurets et al., 1976; Swegle, 1990]. For release paths from the stishovite Hugoniot regime, the zero-pressure density of 3.7 g/cm^3 , $\gamma_0 = 1.0$ and $q = 1.0$ were taken to obtain the equation of state parameters. The release data points were taken from the two Hugoniot pressures of 108 and 71 GPa [Chhabildas and Miller, 1985]. The results are listed in Table 7.

As seen in Fig. 2, the release path of granite from 30 GPa also appears to behave in a similar manner as that proposed for quartz. Figure 6 compares the calculated release paths of granite in the mixed phase regime with the experimental data. The calculations are based on the mixing of the two Hugoniot for the low pressure and high pressure regimes and the frozen mass fraction of the Hugoniot state down to a critical pressure. Below the critical pressure given by $P \text{ (GPa)} = 19.3 - 77 V \text{ (cm}^3\text{/g)}$ the release paths are represented by straight lines on which the formation of diaplectic glasses proceeds.

By applying the finite strain formalism to parts of the release adiabats from the Hugoniot pressures within the mixed phase regime, we obtain the K_{0s} and K'_{0s} for granite.

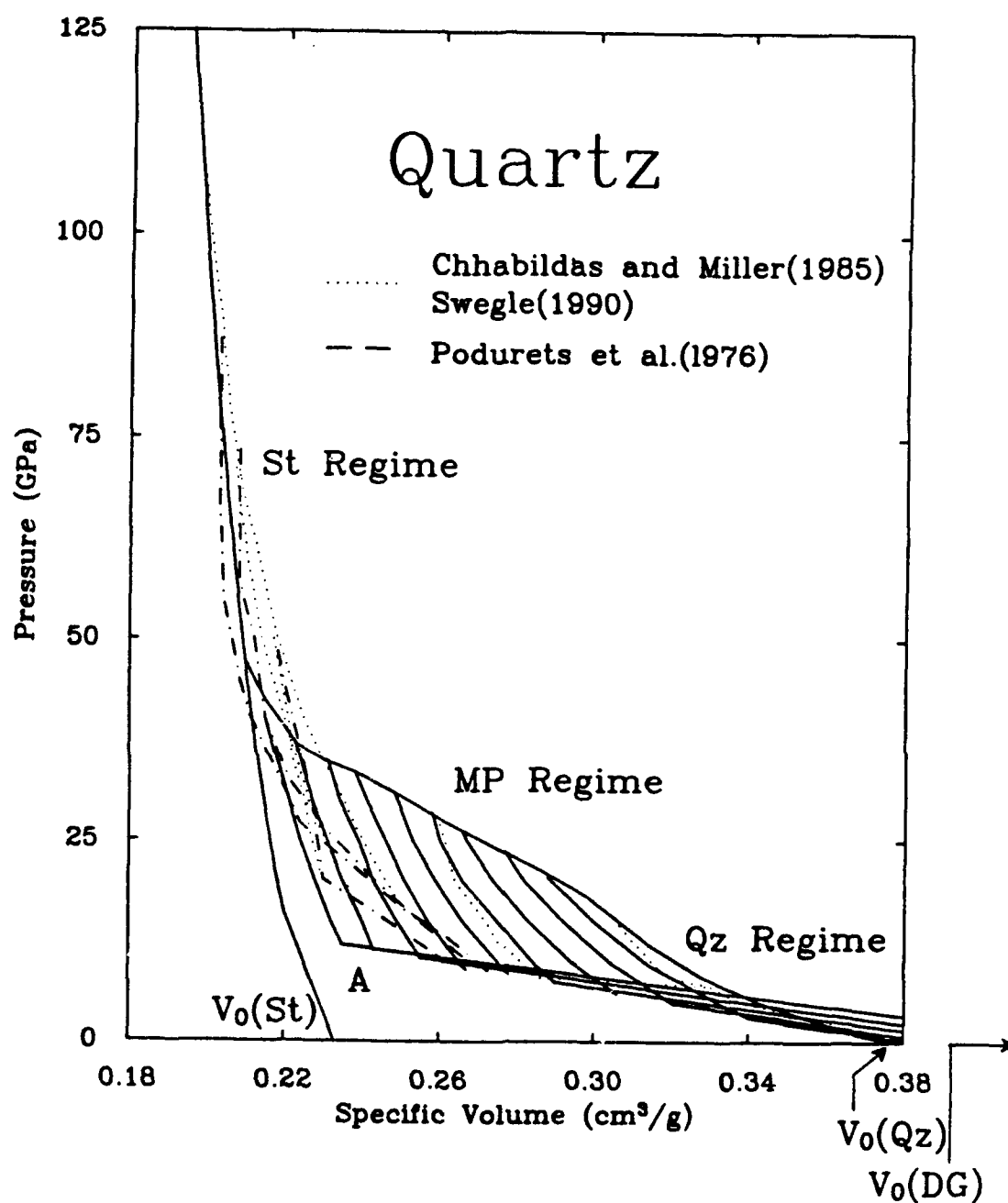


Figure 1-5 Pressure-volume relations for quartz release paths. Dotted and broken curves illustrate experimental data, and solid curves illustrate Hugoniot curves and calculated release paths. Solid curves are computed based on mixed Hugoniots of Qz and St regimes with mass fractions at 0.1 intervals for St. Below critical pressures (Table 7), the release paths are modeled by straight lines. The zero-pressure volume of post-shock quartz shocked above some 50 GPa was taken to be $0.44 \text{ cm}^3/\text{g}$.

Table 7. Summary of Equation of State Parameters of Model Release Adiabats for Quartz

Mass Fraction		Hugoniot States				Birch Murnaghan Relations for Frozen Release Isentrope						
LP	HP	P _H (GPa)	V _H (cm ³ /gm)	E _H (J/gm)	T _H (K)	ρ ₀ (g/cm ³)	K ₀₁ (GPa)	K' ₀₁	P _c (GPa)	ρ ₀₀ (g/cm ³)	E _R (J/gm)	T _R (K)
1.0	0.0					2.65						
0.9	0.1	20.5	.288	912	792	2.75	42	6.3	3.1	2.61	616	614
0.8	0.2	23.5	.277	1175	1017	2.87	47	6.6	5.0	2.56	721	753
0.7	0.3	26	.266	1443	1232	2.99	50	6.9	6.0	2.53	844	874
0.6	0.4	28.5	.258	1696	1502	3.13	58	7.1	7.4	2.49	928	1022
0.5	0.5	31	.248	2000	1768	3.28	64	7.9	8.4	2.44	1086	1148
0.4	0.6	33.5	.238	2328	1982	3.44	73	8.4	9.0	2.41	1232	1301
0.3	0.7	35	.231	2555	2265	3.62	90	8.9	10.5	2.38	1373	1373
0.2	0.8	37	.223	2849	2583	3.82	114	8.8	11.4	2.34	1509	1502
0.1	0.9	40	.215	3240	2995	4.05	203	5.0	12.0	2.30	1687	1673
0.0	1.0					3.7*	991)	5.91)	12*	2.27*		
						3.7*	652)	9.02)	12*	2.27*		

The results are listed in Table 8, together with the zero-pressure density of granite, the critical pressure and density by release path, and the zero-pressure density of post-shock granite. We assumed the same density of 2.27 g/m^3 as in quartz for the proposed diaplectic glass of granite [Stöffler and Hornemann, 1972]. The unloading paths below the critical pressure are associated with relatively large volume changes (Fig. 6). The critical pressure (and density) may vary with the critical pressure of the Hugoniot state [Chhabildas and Miller, 1985]. The parameters are listed in Table 8. For the release path from the high-pressure regime, the equation of state parameters were calculated using the data from 54 GPa Hugoniot pressure [Swegle, 1989]. The results are listed also in Table 8, as well as the zero-pressure density and post-shock granite density used.

According to Swegle [1989] the unloading processes of granite differ from those of quartz. In crystalline quartz, the reverse transformation is well described by the equilibrium reverse transition and by frozen phases until the equilibrium phase boundary is reached, and then the material reverts to the initial phase. This behavior is also the case for fine-grained polycrystalline quartz [Grady et al., 1974]. In the unloading paths of granite, no part is described by the equilibrium reverse transition although they are characterized by frozen high and low pressure phases. The unloading paths of feldspars [Ahrens et al., 1969; Grady and Murri, 1976] illustrate a different behavior from that of quartz, showing a deviation from the frozen high and low pressure phase mixtures toward the low density, well above the expected equilibrium boundary for the high pressure phase (hollandite).

The conditions for formation of diaplectic glasses appear to be restricted to only part of the high pressure phase present in the Hugoniot state which reverts a disordered diaplectic glass via solid-solid transition. Shock-melted glasses have been also recognized (e.g. Stöffler and Hornemann [1972]). The formation of shock-melted glasses, characterized by closer relation of the physical properties to normal glasses quenched from melt, requires much higher shock pressures and consequently higher shock temperatures. The release adiabat for the shock-melt state must be quite different from the release adiabats

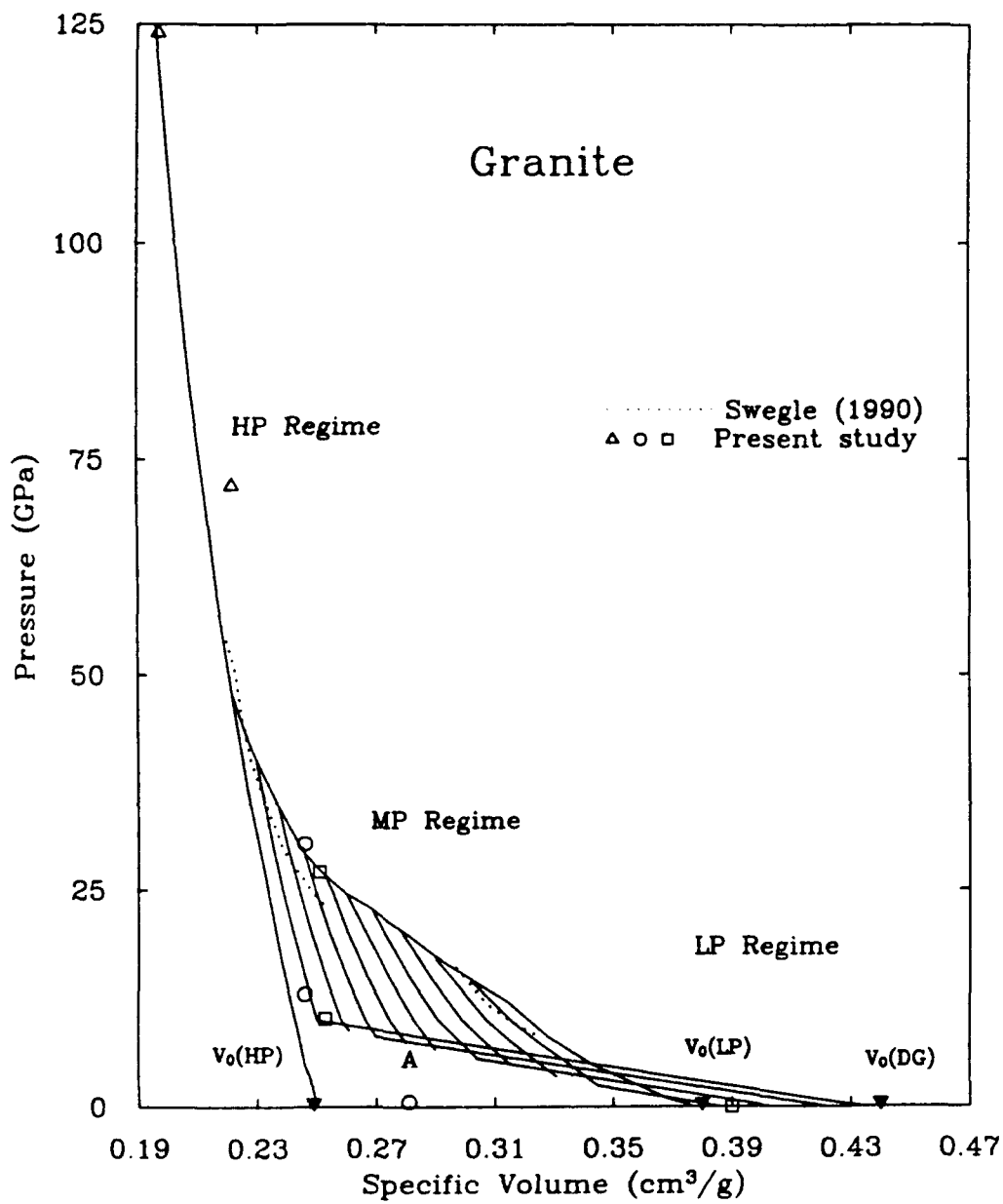


Figure 1-6 Comparison of pressure-volume relations for measured granite release paths with the model calculations. HP-high-pressure, LP = low pressure, MP = mixed phase, and DG = diaplectic glass.

Table 8. Summary of Equation of State Parameters of Model Release Adiabats for Granite

Mass fraction	Hugoniot State		Birch-Murnaghan relations for frozen release isentrope			Critical pressure P_c (GPa)	Final density ρ_{∞} (g/cm ³)	Final		
	P_H (GPa)	V_H (cm ³ /gm)	E_H (J/gm)	T_H (K)	ρ_0 (g/m ³)			K_{0s} (GPa)	K'_{0s}	E_R (J/gm)
LP	HP									
1.0	0.0				2.63					
0.9	0.1	14.5	.302	566	615	42	5.9	2.4	395	492
0.8	0.2	17	.290	765	763	45	6.4	3.5	497	587
0.7	0.3	20	.279	1012	955	49	6.9	5.0	622	697
0.6	0.4	22.5	.269	1249	1152	55	7.5	5.6	725	811
0.5	0.5	24.5	.260	1470	1326	62	8.9	6.6	845	896
0.4	0.6	26.5	.253	1683	1545	73	8.8	7.4	937	1003
0.3	0.7	30	.245	2022	1886	91	9.2	8.1	1063	1186
0.2	0.8	35	.237	2501	2417	120	9.3	8.8	1206	1465
0.1	0.9	40	.230	3004	2943	184	7.8	10.0	1400	1713
0	1.0				3.7*	205 ¹⁾	0.56 ¹⁾	10*		2.27*

1) Calculated on the granite release data from the shock pressure of 84 GPa [Chhabildas and Miller 1985].
* assumed.

discussed here. There appears no significant change in the unloading behavior for quartz release paths observed up to the Hugoniot pressure of 108 GPa [Chhabildas and Miller, 1985]. This is consistent with the shock temperature measurements of quartz to support the presence of crystalline stishovite without melting up to a pressure of about 110 GPa [Lyzenga et al., 1983] although the shock equation of state for quartz at much higher pressures reveals some phase transformation [Trunin et al., 1970].

For anorthite glass, the adiabatic releases from Hugoniot pressures up to 40 GPa are consistent with the frozen high-pressure and low-pressure phase mixture [Boslough et al., 1986]. The releases from much higher shock pressure than 90 GPa, however, showed a significant change of the release adiabat slope. It seems to be due to melting according to a proposed phase diagram for anorthite [Schmitt and Ahrens, 1983]. For the other feldspars, no significant change of the adiabatic release behavior was observed at least up to the Hugoniot pressure of 46 GPa [Ahrens et al., 1969; Grady and Murri, 1976]. The results of investigations of post-shock samples reveals slightly lower pressure values for formation of shock-fused glasses, i.e. about 43 GPa for feldspars and 50 GPa or 40 GPa for quartz [Stöffler and Hornemann, 1972; Tattévin et al., 1990].

P-V-E Relations for Quartz and Granite

The pressure-volume unloading paths depicted in Figures 4-6 provided additional information regarding energies and hence temperatures achieved during the shock and subsequent release process. This offers a means to further test the inferred release paths by comparing shock and post-shock temperatures with available data and theoretical expectations. The specific energy due to compression is obtained from conservation of energy across the shock front:

$$E_H = P_H(V_o - V) / 2 \quad (11)$$

The Hugoniot energies for quartz and granite are listed in Tables 8 and 9 for points in the mixed phase region corresponding to increasing fractions of frozen high pressure

material. Integration of the P-V release paths in Figures 4-6 yields the total energy under the release isentrope, E_r . These are also listed in Tables 8 and 9 for quartz and granite, respectively. Residual (post-shock) temperatures were calculated from:

$$T_r = T_o + (E_H - E_r) / \bar{C}_v \quad (12)$$

where \bar{C}_v is the average specific heat at constant volume [Robie et al., 1978] over the temperature interval T_r - T_o .

The resulting post-shock temperatures for quartz and granite are contained in Tables 7 and 8 and Figure 7. For quartz, the maximum temperature achieved is 1673 K which is less than the 1 atm. melting temperature of SiO_2 (1996 K). The maximum temperature achieved in granite is similar (1713 K at 40 GPa). We therefore infer that at pressures between 15-40 GPa both quartz and granite remain solid upon isentropic unloading. As discussed above, Chhabildas and Miller [1985] infer that release from pressures above 50 GPa results in a high-density quartz liquid. The transition energy associated with the transformation of the high pressure component to diaplectic glass can be estimated using the quartz to fused quartz transition energy (123 J/gm) for the transforming high-pressure phase fraction. The effect of including this term is to produce a slight decrease in the calculated post-shock (and shock) temperature (cf: Figure 8).

Also shown in Figure 7 are experimentally determined post-shock temperatures for quartz [Raikes and Ahrens, 1979] and stishovite [Boslough, 1988; Chhabildas and Miller, 1985]. The present results are in good agreement with the highest pressure quartz data but are ~500 K colder than the stishovite data extrapolated to the top of the mixed phase region (~40 GPa). The results of Chhabildas and Miller [1985], and possibly Boslough [1988] as well, do not represent complete unloading and may therefore overestimate the residual temperature. The calculation of Wackerle [1962] based on the Mie-Gruneisen Equation predicts lower temperatures in the mixed phase region and a PT slope in the stishovite field which is much steeper than suggested by the experiments.

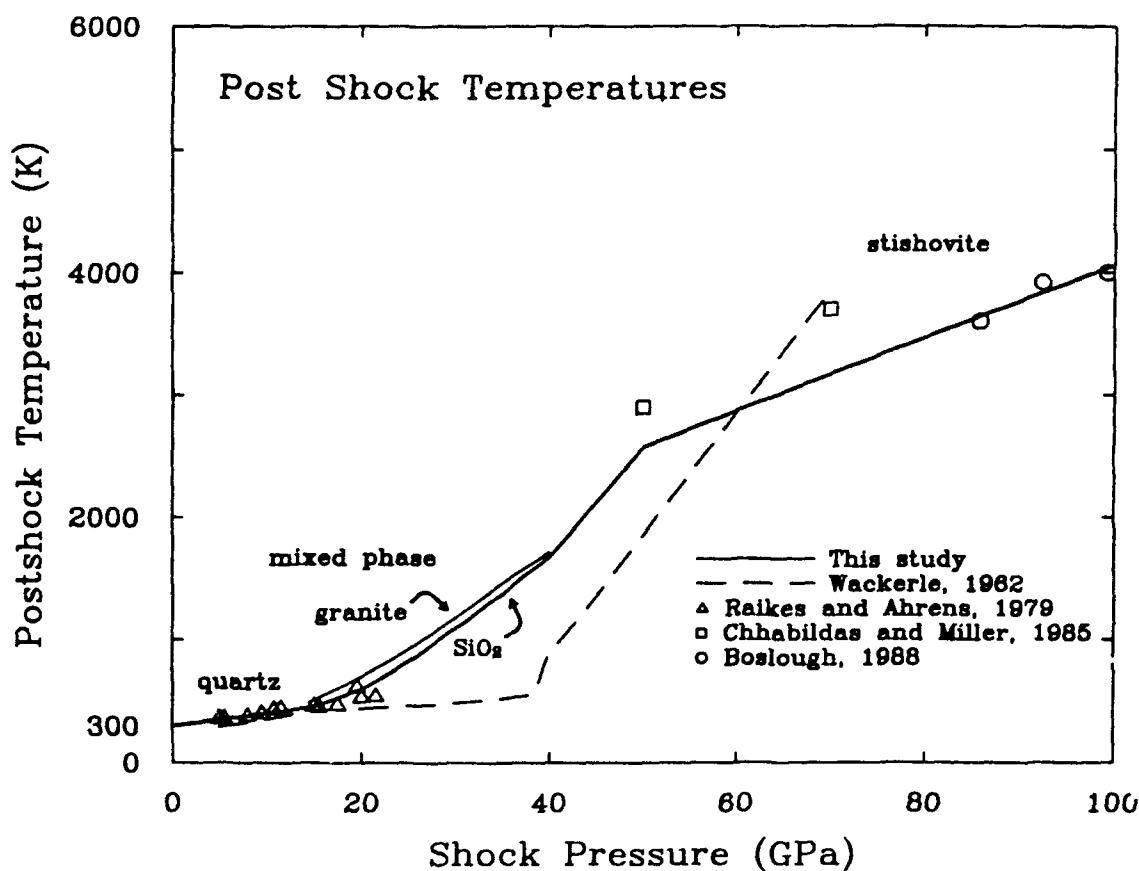


Figure 1-7

Post-shock temperatures for quartz and granite plotted as a function of peak shock pressure. The heavy solid line represents preferred values for post shock temperatures in quartz between 0 and 100 GPa. Post shock temperatures calculated for granite in the mixed phase region are shown as the solid line. Also shown are experimental determinations for SiO₂ in both the quartz and stishovite stability fields. The data sets of Raikes and Ahrens [1979] and Boslough [1988] are from measurements of post-shock radiation. The data of Chhabildas and Miller [1985] represent calculated values determined from measured wave profiles and the Mie-Gruneisen equation. The dashed line is the calculation of Wackerle for SiO₂.

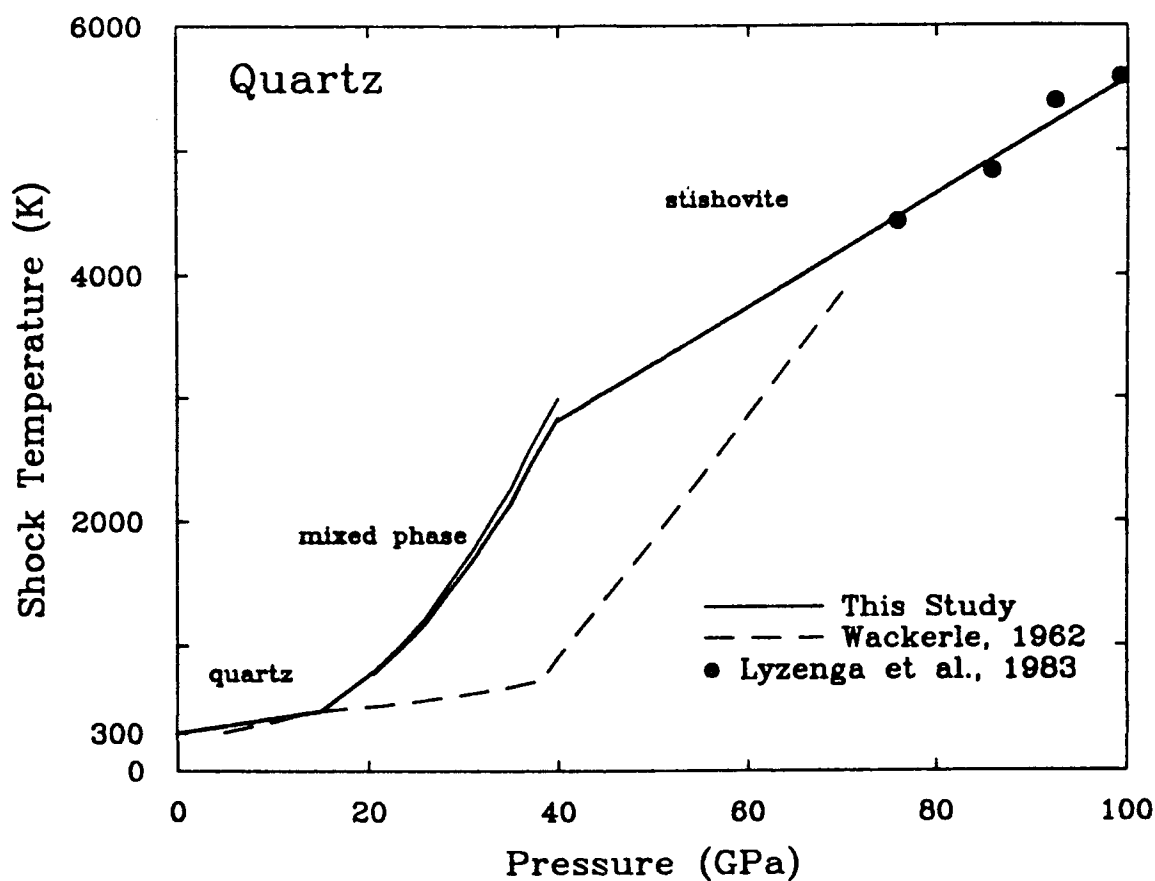


Figure 1-8 Shock temperatures in SiO₂ as a function of shock pressure. The heavy solid line represents preferred values of shock temperature in the low pressure, mixed phase, and high pressure regimes of SiO₂. The steep P-T slope calculated for the mixed phase region in this study contrasts with the shallow slope calculated by Wackerle [1962]. The data of Lyzenga et al. [1983] were obtained from pyrometer measurements. The present results agree well with the extrapolated trends from this data set.

The temperature decrease along the isentropic path from the shock state to complete unloading can be used to infer the Hugoniot temperature. Using the Mie-Gruneisen equation of state together with the assumption that γ/V is constant results in the following:

$$T_H = T_r \exp \left[\frac{\gamma_o}{V_o} (V_r - V_H) \right] \quad (13)$$

where the subscript H refers to Hugoniot conditions, o to the initial state, and r to the post-shock state. Hugoniot temperatures calculated in this manner are displayed in Tables 7 and 8 and Figures 8 and 9. The incorporation of the quartz - fused quartz phase transition energy has only a small effect (Figure 8). Temperatures in the mixed phase region are found to increase much more rapidly with pressure than those in either the low pressure phase or high pressure phase. This is due to large increases in energy caused by the large volume change associated with the transformation. It is interesting to note that the calculated temperature for SiO_2 at the top of the mixed phase region is very similar to the extrapolated value for stishovite at that pressure based on the measurements of Lyzenga et al. [1983]. This contrasts with the calculation of Wackerle [1962] who predicted a very shallow PT slope in the mixed-phase region but a much steeper slope than observed in the stishovite region. Figure 9 demonstrates that shock temperatures for quartz and granite are very similar in the mixed-phase region. The calculated temperature for granite at the top of the mixed-phase region is ~700 K higher than that calculated for the high pressure phase at nearly the same pressure. Temperatures for the high pressure phase were obtained using the approach of McQueen et al. [1970] and the classical limit of $3R$ for the specific heat. These results demonstrate that the present model for both quartz and granite are consistent from an energetic viewpoint and produces temperatures in reasonable accord with expected behavior.

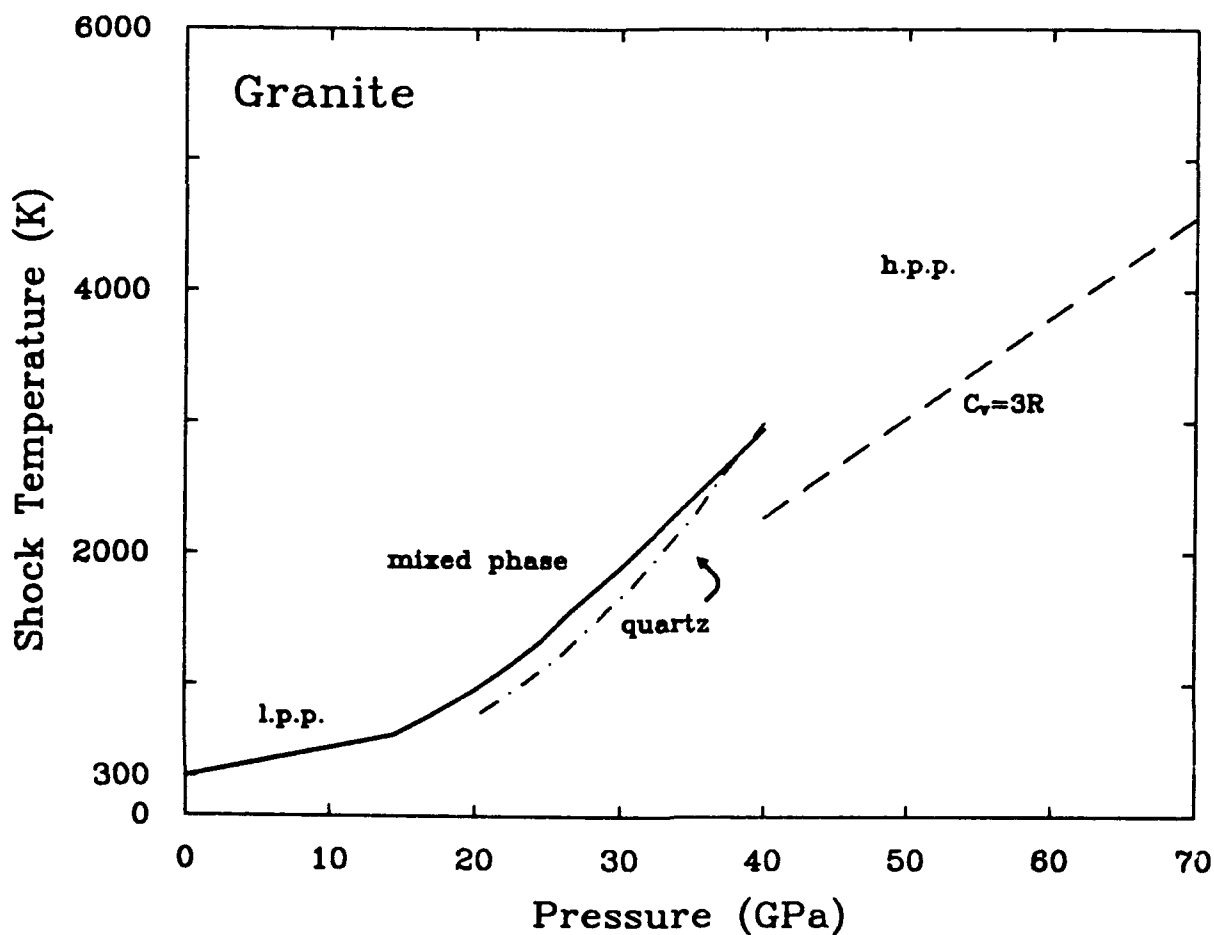


Figure 1-9 Shock temperatures in granite as a function of shock pressure. Preferred values of the shock temperature of granite in the low pressure and mixed phase regions are shown by the heavy solid line. In the mixed phase region, granite temperatures are similar to those in SiO₂. The temperature at the top of the mixed phase region is ~700 K lower than calculated values for the high pressure phase of granite assuming $\gamma_0 = 1$ and $C_v = 1.19$ J/gmK.

CONCLUSION

New equation of state data for granite have been obtained and combined with the Westerly granite data of McQueen et al. [1967]. the shock equation of state can be described by two linear relations, $U_s = 4.70 + 0.46 U_p$ (km/sec) for a range of U_p from 0.7 to 2 km/sec and $U_s = 2.66 + 1.49 U_p$ for a range of U_p from 2 to 5 km/sec. These shock equations of state are comparable with other data previously determined for various granites. The third order Birch-Murnaghan equation of state parameters are $K_{os} = 57$ GPa and $K'_{os} = 1.8$ for the low-pressure regime ($\rho_o = 2.63$ g/cm³) and $K_{os} = 304$ GPa and $K'_{os} = 1.2$ for the high-pressure regime ($\rho_o = 4.02$ g/cm³). These parameters lie between those of quartz and feldspar in the low-pressure regime, and between those of stishovite and the hollandite form in the high-pressure regime.

For the release adiabats from the mixed phase regime, the mixed Hugoniot model is applied and compared with experimental data. In this model, the release adiabats are calculated for the high-pressure and low-pressure phase mixture with the same mass fraction as at the Hugoniot state to critical pressures given by $P(\text{GPa}) = 19.3 - 77 V$ (cm³/g).

Further releases below the critical pressures are associated with large volume changes related to formation of diaplectic glasses as quenched modifications of the high-pressure fractions.

Based on the measurements of partially released states of granite as well as quartz shocked in the high-pressure regime ($P > 50$ GPa), it is proposed that the high-pressure form relaxes isentropically to a metastable, intermediate phase characterized by dense, highly-disordered material. This material is subsequently quenched to diaplectic glass. The process of diaplectic glass formation differs from that of shock-fused glass which can result only from much higher Hugoniot pressure. The release adiabat associated with the shock-fused glass formation must be distinguished from the release adiabat discussed in the present study. The inferred release curves from the mixed region for quartz yield Hugoniot

temperatures which are considerably higher than those of Wackerle [1962], but are consistent with the data of Lyzenga et al. [1983]. Moreover, the post shock temperatures predicted agree closely with the data of Raikes and Ahrens [1979] at low pressures and the data of Chhabildas and Miller [1985], and Boslough [1988] at higher pressures. These agreements lend further support to the release model developed here.

CHAPTER 2

SHOCK WAVE EQUATION OF STATE OF
MUSCOVITE

Toshimori Sekine¹, Allan M. Rubin², and Thomas J. Ahrens

Seismological Laboratory
California Institute of Technology
Pasadena, CA 91125

¹ Permanent Address: National Institute for Research in Inorganic Materials, Tsukuba, Ibaraki 305, JAPAN.

² Present Address: Dept. of Geological Sciences, Brown University, Providence, R.I., 02912.

INTRODUCTION

Hugoniot equation of state of minerals and rocks provide the basis of describing shock wave propagation from intense explosions in the Earth, the effects of meteorite impact on the Earth and the planets, as well as contributing to our knowledge of the Earth's interior and the accretion of the Earth. Small amounts of water in the interior can be requested in hydrous minerals such as serpentine, brucite, amphiboles and micas. These hydrous minerals may play a critical role in the evolution of the interior, as well as in the physical and chemical nature of the mantle. Muscovite is also among the potassium-bearing minerals that could influence the chemistry of mantle.

Since there are no previous equation of state data available for the most common crustal hydrous mineral, muscovite, it was the subject of the present study. The present data complement recent other shock wave studies of the hydrous minerals [Duffy et al., 1991; Tyburczy et al., 1990].

Previously, Cummings [1968], Short [1968b], Short [1968a], Hörz and Ahrens [1969], and Lambert and Mackinnon [1984] investigated the post-shock response of muscovite from laboratory experiments and from material in the vicinity of underground explosions. They observed characteristic features such as kinking, mosaic extinction, melting, and vesiculation. These field and laboratory studies lacked detailed knowledge of the equation of state of muscovite. Moreover, studies of the equation of state of granite rocks and their syntheses require shock wave data for constituent minerals.

EXPERIMENTAL

The natural muscovite of the present study was from Methuen Township, Ontario (Harvard University Mineralogical Museum, Cat. #112791). The composition is listed in Table 1. The apparent size is about 40x50x2mm. The average crystal density, determined by Archimedean method was $2.8346 \pm 0.0026 \text{ g/cm}^3$. This is in good agreement with x-ray

Table 1. Chemical Composition (wt %) of muscovite

	a	b	c	d	e
SiO ₂	45.87	45.20	45.41	45.26	47.30
Al ₂ O ₃	38.69	38.46	38.52	38.40	36.05
Na ₂ O	0.64	0.60	0.62	--	0.21
K ₂ O	10.08	10.44	10.91	11.82	10.77
H ₂ O	4.67	4.64	4.53	4.52	4.9
Total	99.95	99.34	99.99	100.00	99.23

- a. Hurlbut, C. S. Jr. [1956] Remainder - not listed is 0.10 wt % MgO.
- b. Eugster et al.[1972] Remainder - not listed are FeO, Fe₂O₃, MnO, Li₂O₃, TiO₂, etc. and summed to be about 0.4 wt. %
- c. Calculated from present idealized muscovite (K_{0.92}Na_{0.08}) Al₃Si₃O₁₀(OH)₂.
- d. Calculated from pure muscovite KAl₃Si₃O₁₀(OH)₂.
- e. Vaughan and Guggenheim [1986].

density measured for a muscovite with a similar composition [Vaughan and Guggenheim, 1986]. The entire sample was imbedded in epoxy resin and cut into rectangular aliquots (7 x 13 x 2mm).

Shock loading was conducted with the Caltech 25mm two-stage light gas gun using metal flyer plate bearing projectiles to impact samples at speeds of up to 6.3 km/sec. Projectile velocity just prior to impact was determined by double exposure flash x-ray photography using two 15 nsec flash x-ray sources and electronic time interval counters [Jeanloz and Ahrens, 1977]. Shock wave velocities in the target and buffer materials were determined by recording the destruction time of the mirrors through an image converter streak camera and xenon light source [Ahrens, 1987]. A 40-mm propellant [Ahrens et al., 1969] was used to accelerate lexan projectiles fitted with either Cu or Ta flyer plates to velocities up to 2.4 km/sec. Projectile velocities were measured using flash x-ray images. Sample and buffer mirror shock velocities were obtained from observations of shock-induced loss of mirror reflectivity at successive reflective surfaces as recorded by a rotating-mirror streak camera.

The flyer and driver plates used in this study were the same to obtain the symmetric impact conditions. The assumed equation of state parameters are listed in Table 2. The particle velocity behind the shock front and pressure-density states were calculated through the impedance match method and the Rankine-Hugoniot equations, respectively. Uncertainties were determined by standard error propagation techniques [Jackson and Ahrens, 1979].

Partial release states were obtained by measuring the shock wave transit time through low impedance buffers in contact with the sample. The pressure and particle velocity at the buffer-sample interface were determined from the measured shock velocity and the known equation of state for the buffer material (lexan). An upper bound for the density of the partial release state can be calculated by integrating the Riemann integral over a linear pressure-volume (P-V) path [Lyzenga and Ahrens, 1978]. For all of the shots, streak

camera cutoffs could be observed for the lexan arrival mirrors mounted on the rear sample surface.

In several experiments, polystyrene foam buffers, as well as lexan mirrors, were mounted on the rear sample surface to observe partial release states. Table 2 summarized the shock wave equation of state parameters for flyers, drivers, and buffers used in the present study.

RESULTS AND DISCUSSION

Present experimental results and calculations are listed in Table 3 for the Hugoniot and partial release states determined.

Hugoniot States

Peak shock pressures achieved ranges between 20 and 142 GPa. The relationship between the shock velocity (U_s) and particle velocity (U_p) is presented in Fig. 1. The data set can be described by a linear regression of the seven points:

$$U_s = C_0 + S U_p \quad (7)$$

where the C_0 is fitted to be 4.63 ± 0.12 km/sec and the constant S is to be 1.27 ± 0.04 . The C_0 determined is the same within experimental errors as the average value measured by Brillouin scattering technique for a single crystal muscovite, of which composition is similar to ours [Vaughan and Guggenheim, 1986]. The parameters C_0 and S do not change significantly ($C_0 = 4.62 \pm 0.12$ and $S = 1.27 \pm 0.04$) upon also employing the acoustic value of $C_0 = 4.56 \pm 0.40$ to the data set. The zero-pressure bulk modulus (K_{0s}) and the first pressure derivative (K'_{0s}) can be calculated using:

$$K_{0s} = \rho_0 C_0^2 \quad (8)$$

$$K'_{0s} = 4S - 1 \quad (9)$$

They are 60.5 ± 3.1 GPa and 4.1 ± 0.2 , respectively.

Pressure-density states attained in the shock compression of muscovite are depicted in Fig. 2, and compared with the model calculations based upon the assumed Hugoniots for

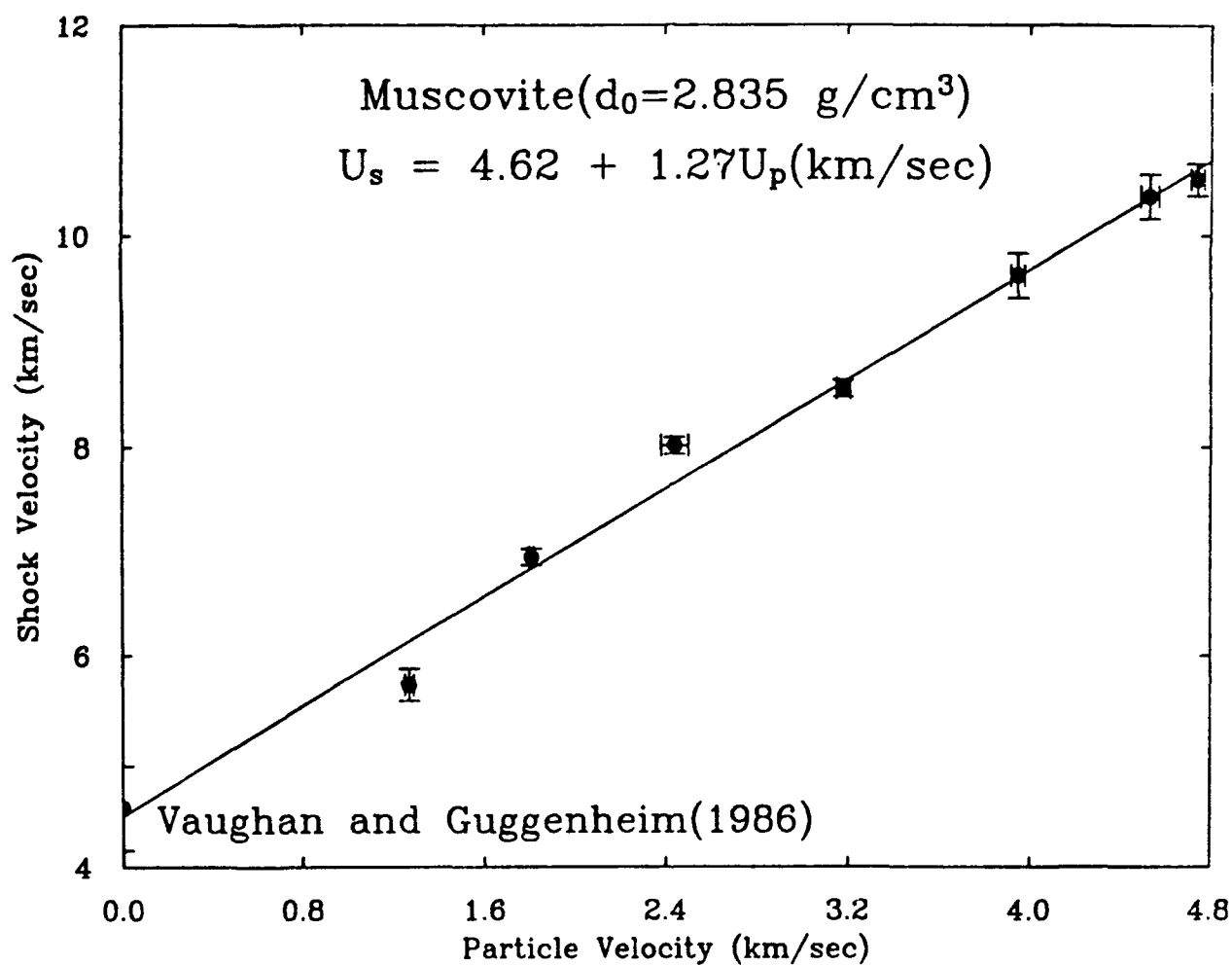


Figure 2-1. Shock velocity (U_s , km/sec) versus particle velocity (U_p , km/sec) for muscovite. Shock velocity at $U_p=0$ is within the range of acoustic bulk sound velocity for muscovite [Vaughan and Guggenheim, 1986].

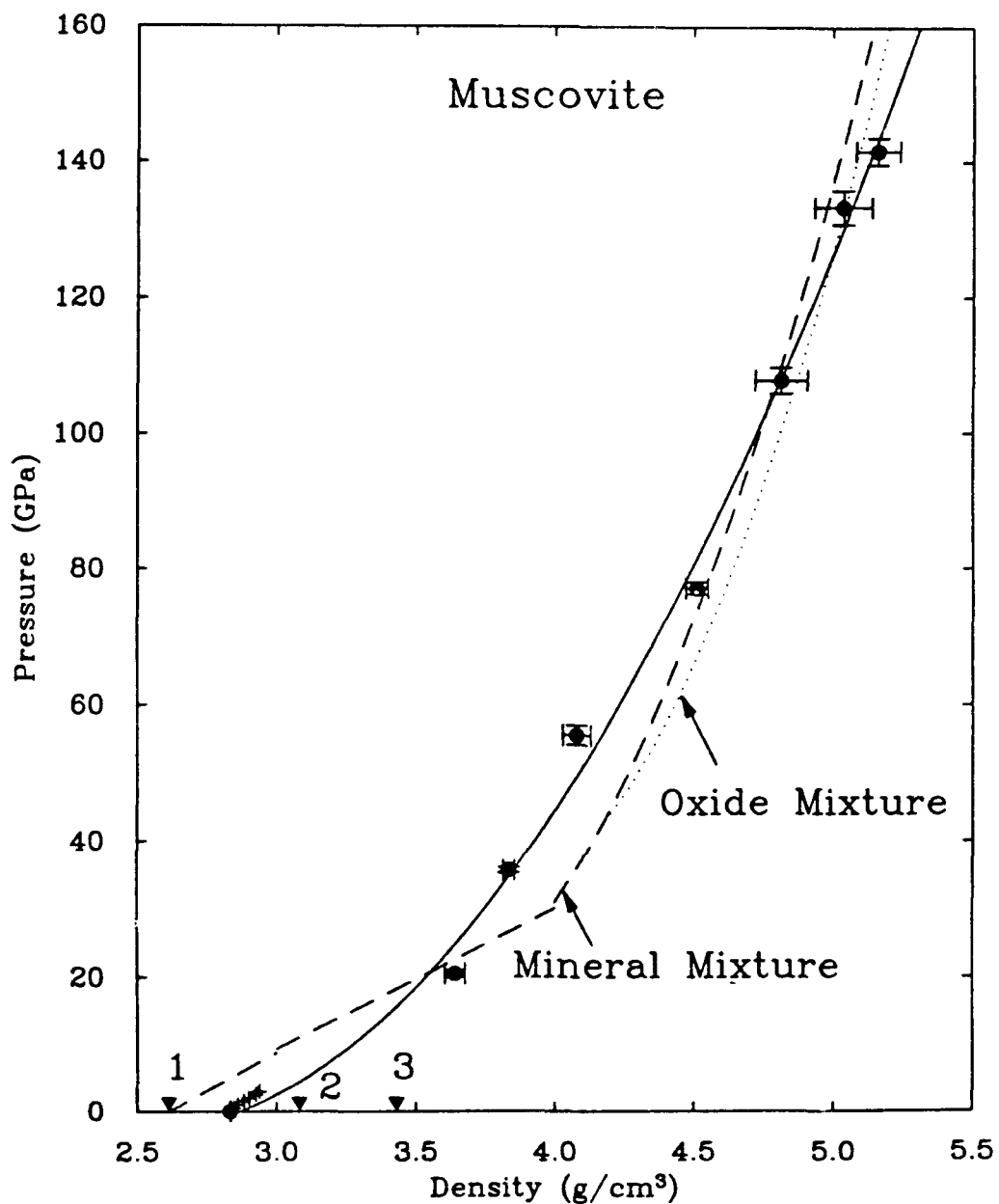


Figure 2-2. Pressure-density relations for Hugoniot state of muscovite. Solid circles are from present study, broken curve is for mineral mixtures, and dotted curve assumes oxide mixture model [Telegin et al., 1980]. Pluses are for the static compression for muscovite [Bridgman, 1949]. The zero-pressure densities at points 1, 2 and 3 correspond to mixtures of orthoclase + $\text{Al}_2\text{O}_3 + \text{H}_2\text{O}$, of wadeite + kyanite + $\text{Al}_2\text{O}_3 + \text{H}_2\text{O}$, and KAlSi_3O_8 (hollandite) + $\text{Al}_2\text{O}_3 + \text{H}_2\text{O}$, respectively.

Table 2. Shock equation of state parameters for flyers, drivers, and buffers used in the present study

Material	Initial density (g/cm ³)	Us-Up relation (km/sec)	Measured range of Up (km/sec)	Ref.
Cu	8.92	$U_s = 3.91 + 1.51 U_p$	0.2~4.2	1
Al, 1100	2.712	$U_s = 5.38 + 1.34 U_p$	1.5~5.1	1,2,3
Ta	16.656	$U_s = 3.43 + 1.19 U_p$	0.8~4.9	1
lexan	1.193	$U_s = 2.419 + 1.321 U_p$	3.2~5.2	1
		$U_s = 2.449 + 1.498 U_p$	0.4~28.0	
polystyrene foam	0.055	$U_s = 0.243 + 1.118 U_p$	0.2~5	1

1. Marsh [1980]
2. Mitchell and Nellis [1982]
3. Brown and Shaner [1984]

non-reactive mineral mixture (e.g. KAlSi_3O_8 (orthoclase to 30 GPa and hollandite above 30 GPa) + $\text{Al}_2\text{O}_3 + \text{H}_2\text{O}$) [Al'tshuler and Sharipdzhanov, 1971] and oxide mixture (e.g. $\text{K}_2\text{O} + \text{Al}_2\text{O}_3 + \text{SiO}_2 + \text{H}_2\text{O}$) [Telegin et al., 1980]. In the mineral mixture model calculations, the total volume (V) at a given pressure is calculated to be

$$V(P) = \sum_i m_i v_i(P) \quad (10)$$

where m_i is a fraction of the individual constituent mineral i with a volume of v at the pressure P . The Hugoniot for KAlSi_3O_8 , Al_2O_3 , and H_2O can be found in the literature [Ahrens et al., 1969; Marsh, 1980; Mitchell and Nellis, 1982; Simakov et al., 1974]. Since the Hugoniot for alkali feldspars and plagioclase are insensitive to composition, the corresponding feldspar to the present muscovite can be taken to be microcline for which Hugoniot has been determined up to 191 GPa [Simakov et al., 1974]. In Figure 2, the static compression data [Bridgman, 1949] are added to describe the low pressure region. However, the shock wave data appear to indicate greater compressibility than the static data. Formal fits for equation of state parameters from the 4 GPa static data yields the values of $K_{OS} = 108 \pm 5$ GPa and $K_{OS}' = 22 \pm 4$.

Telegin's model of oxide mixture Hugoniot can be applied to synthesize the muscovite data in an approximate range of particle velocity from 2 to 5 km/sec [Telegin et al., 1980]. This corresponds to a pressure range of 40 to about 150 GPa. For multi-component systems,

$$U_s = C_0(\rho_0, Z) + S(\rho_0, Z) U_p \quad (11)$$

where parameters $C_0(\rho_0, Z)$ and $S(\rho_0, Z)$ are given from the initial density (ρ_0) of rocks and weight percentage (Z) of oxide constituents in rocks.

$$C_0 = a_0 + a_1 \rho_0 + \sum_i Z_i a_i \quad (12)$$

$$S = b_0 + b_1 \rho_0 + \sum_i Z_i b_i \quad (13)$$

where constants a_0, a_1, a_i and b_0, b_1, b_i have been obtained statistically [Teagin et al., 1980].

As seen in Fig. 2, the measured densities are in good agreement with the two model calculations in the pressure range of about 80 to 140 GPa.

The shock wave data are reduced to an isentrope by applying the third order Birch-Murnaghan equation of state. A formalism is the finite strain model to analyze the Hugoniot data [Ahrens and Jeanloz, 1987; Heinz and Jeanloz, 1984; Jeanloz, 1989].

The Eulerian strain f is expressed as

$$f = \frac{1}{2} \left[\left(\frac{\rho}{\rho_0} \right)^{2/3} - 1 \right] \quad (14)$$

where ρ and ρ_0 are Hugoniot and ambient densities, respectively. The normalized pressure F_{HS} is given by

$$F_{HS} = \frac{1 - \frac{\gamma}{2} [(1 + 2f)^{3/2} - 1]}{3f(1 + 2f)^{3/2} [1 + (2 - 1.5\gamma)f]} P_H \quad (15)$$

where γ is the Gruneisen parameter and P_H is the Hugoniot pressure.

$$\gamma = \gamma_0 \left(\frac{\rho_0}{\rho} \right)^q \quad \text{where} \quad \gamma_0 = \frac{\alpha K_{os}}{C_p \rho_0} \quad (16)$$

α is the volume coefficient of thermal expansion and C_p is the specific heat at constant pressure. The value of α for muscovite is unknown and we use $\alpha = 35 \times 10^{-6} \text{ K}^{-1}$ from muscovite [Guggenheim et al., 1986]. C_p is assumed to be $C_v = 0.818 \text{ J/g}\cdot\text{K}$ which is given

by Robie et al. [1978]. By using $K_{OS}=60.5\pm3.1$ GPa from the shock wave equations of state, the value of 0.72 ± 0.04 is calculated for γ_0 . The q values of 1.0 ± 1.0 were taken in the present analyses. Without a phase transformation the internal energy of transformation, $E_{tr} = 0$, and a linear least squares fit using Eq. (17) to the combined data set, yields the parameters of $K_{OS}=52\pm14$ GPa and $K_{OS}'=3.2\pm0.3$.

$$F'_{HS} = F_{HS} + \Delta F_{tr} = K_{OS}(1 - 2\xi f_{3H} + \dots) \quad (17)$$

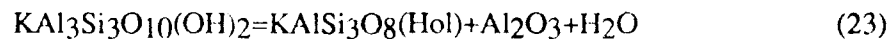
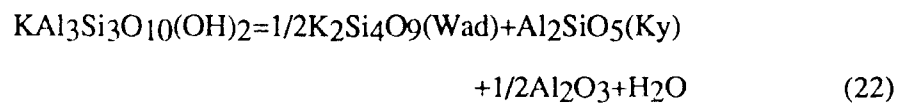
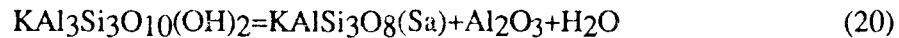
where

$$\Delta F_{tr} = \left(\frac{E_{tr}}{V_0} \right) \frac{\gamma}{3f[1 + (2 - 1.5\gamma)f]} \quad (18)$$

and

$$f_{3H} = \frac{f[1 + (2 - \gamma)f]}{1 + (2 - 1.5\gamma)f} \quad (19)$$

The present shock wave data of muscovite do not indicate any strong evidence for a rapid transformation to a high-pressure phase in the U_s - U_p or pressure-density plots. However, the present data cannot exclude the phase transitions which are associated with small volume changes. There are several possible decomposition reactions for muscovite ($KAl_3Si_3O_{10}(OH)_2$) as follows:



where Sa=sanidine, SaHy=sanidine hydrate, Wad=wadeite [Kinomura et al., 1975], Ky=kyanite, and Hol=hollandite (Ringwood et al., 1967). The calculated volume changes

associated with the above reactions are 11.92, -0.27, -11.52, and -24.64 cm³/mol at the zero-pressure, respectively. The initial densities are shown in Fig. 2 for the decomposition products. Reaction (20) is limited to high temperatures and relatively low pressures [Chatterjee and Johannes, 1974], and reaction (21) is also limited to relatively low temperatures and pressures [Seki and Kennedy, 1964].

To understand the stability of muscovite, a phase diagram was constructed using available thermodynamic data for muscovite and its decomposition products. Thermodynamic data are taken from Robie et al. [1978] and are extrapolated outside their applicability to muscovite above 1000 K. Thermodynamic functions for H₂O were taken from Halbach and Chatterjee [1982]. Gibbs' free energy values for wadeite, K₂Si₄O₉, and KAlSi₃O₈ (hollandite) were computed for the following equilibrium reactions:



and



We approximated the boundary conditions as follows [Liu and Bassett, 1986]:

$$P(\text{GPa}) = 6.3 + 0.002T(^{\circ}\text{C}) \text{ for reaction (24)} \quad (26)$$

and

$$P(\text{GPa}) = 8.3 + 0.0035T(^{\circ}\text{C}) \text{ for reaction (25)} \quad (27)$$

where the effects of both temperature and pressure on volumes were neglected as a first approximation. The resultant equilibrium conditions for reaction (23) are expressed as

$$P(\text{GPa}) = 7.8 + 0.0047T(^{\circ}\text{C}) \quad (28)$$

which is shown in Fig. 3.

Temperatures along the Hugoniot were calculated using the method of McQueen et al. [1967]. We integrated the equation:

$$\frac{dT}{dV} = -T \left(\frac{\gamma}{V} \right) + \frac{\frac{dP}{dV}(V_0 - V) + P}{2C_v} \quad (29)$$

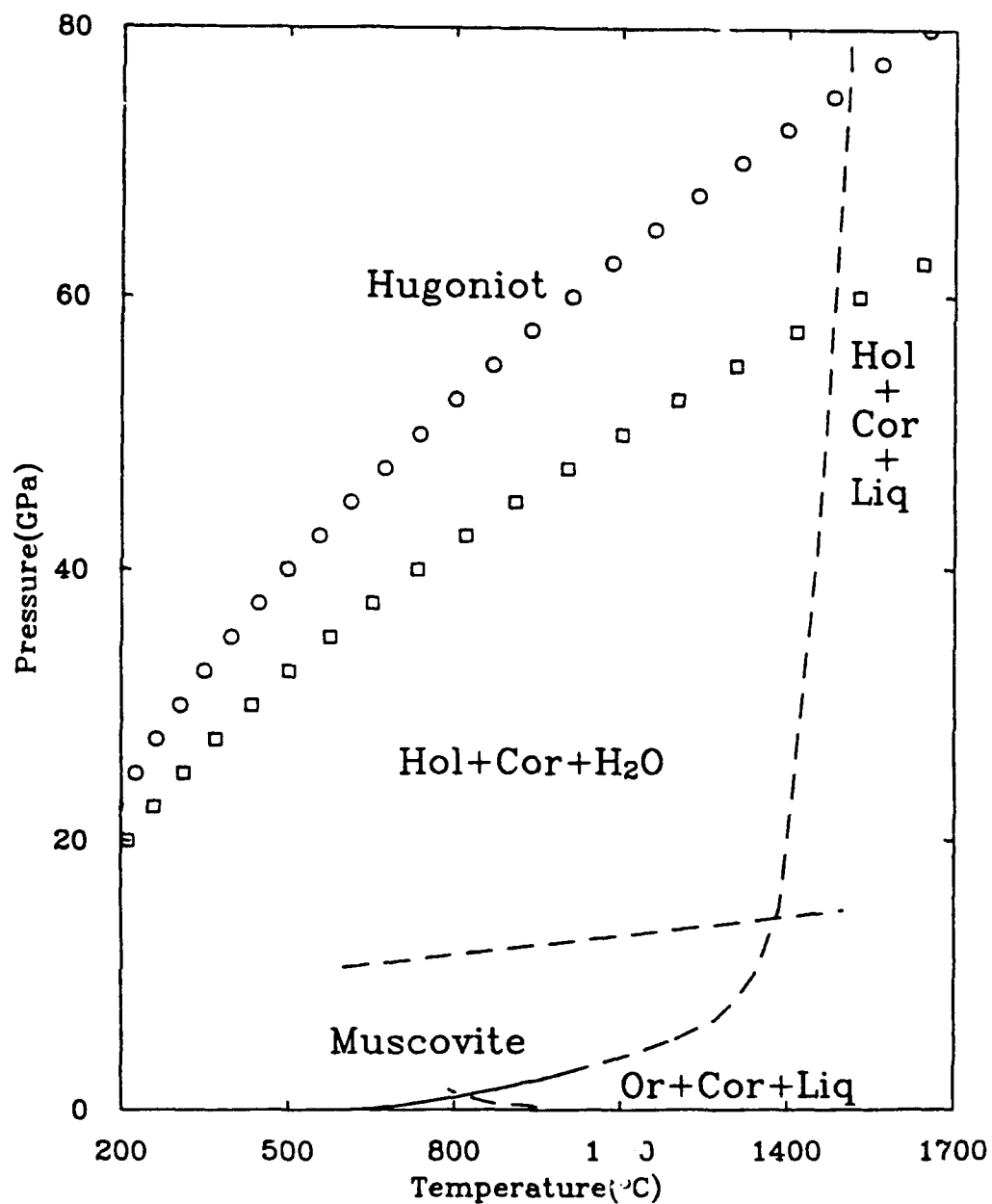


Figure 2-3. Pressure-temperature projection of phase boundaries and muscovite Hugoniot. Circles represent the Hugoniot calculation using the heat capacity at 298K and squares represent those using the value at 1000 K. Abbreviations: Hol=hollandite KAlSi_3O_8 , Cor= Al_2O_3 ; Or=orthoclase and Liq=liquid. Solid curve was experimentally determined by Huang and Wyllie [1973].

and

$$\frac{dS}{dV} = \frac{\frac{dP}{dV}(V_0 - V) + P}{2T} \quad (30)$$

The resulting shock temperatures are shown in Figure 3. The muscovite Hugoniot is expected to intersect the boundary defined by reaction (23) about 8 GPa. However, the present Hugoniot data obtained for muscovite indicate that muscovite remains present at least up to about 60 GPa, where the Hugoniot temperature is about 1000°C. If muscovite decomposes at a lower shock pressure, the Hugoniot is expected to coincide with that of the mineral mixture model above 30 GPa because the constituent KAlSi_3O_8 transforms to the hollandite structure [Ahrens and Liu, 1973; Ahrens et al., 1969].

The equilibrium pressure for reaction (22) involving wadeite phase has a lower pressure than reaction (23). Since there is no indication that transition wadeite occurs in the microcline Hugoniot data, it is hard to discuss the reaction (22) in the intermediate pressure range.

The equation of state parameters of muscovite ($K_{OS}=52\pm4$ GPa, $K_{OS}'=3.2\pm3$) are comparable with those of brucite [Duffy et al., 1991] ($K_{OS}=51\pm4$ GPa, $K_{OS}'=5.0\pm0.4$) and serpentine [Tyburczy et al., 1990] ($K_{OS}=63.5\pm6.7$ GPa; $K_{OS}'=2.75\pm0.62$) which have been recently determined. The elasticity measurement of muscovite by Brillouin scattering technique gave the average bulk sound velocity of 4.56 ± 0.40 km/sec, [Vaughan and Guggenheim, 1986] which corresponds to a bulk modulus of 59.0 ± 5.2 GPa. This value is consistent with our results. A finite strain analysis of the tremolite Hugoniot data below about 65 GPa [Simakov and Trunin, 1980] yields the $K_{OS}=76\pm6$ GPa and $K_{OS}'=5.1\pm0.5$. The static compression data of portlandite $\text{Ca}(\text{OH})_2$, which is isomorphous with brucite yields $K_{OS}=37.8\pm1.8$ GPa and $K_{OS}'=5.2\pm0.7$ at room temperature [Meade and Jeanloz, 1990]. It is noteworthy that these hydrous minerals vary greatly in their water content from about 2 wt % of tremolite to about 30 wt % of brucite, but that they have similar equation of state parameters.

Partial Release States

Measured partial release states for muscovite are listed in Table 3 and depicted in Fig. 4. Although the shock equation of state for lexan (buffer material) has been determined only in the Up range up to about 5.2 km/sec [Marsh, 1980], we used a single linear regression of the high pressure portion to calculate the observed release states. The release path observed from the lowest Hugoniot pressure about 20 GPa displays an irregular shape. Taking into account the experimental errors (Table 3), the shock wave may have been attenuated in polystyrene, causing us to measure too low a shock velocity in the buffer. The partial release states obtained from the Hugoniot pressures below 110 GPa indicate that the adiabatic release paths are steeper or almost have the same slopes in the Hugoniot density-pressure plane. These steep paths have been interpreted as indicating retention of the denser high-pressure phase during the release (e.g. Swegle [1990]). As seen in Fig. 4, however, the release paths from the Hugoniot pressures of 130 to 140 GPa indicate slightly shallower paths than those from the lower pressures. The shallower paths mean the expected devolatilization during release. The local slope of isentropic expansion of a point on the Hugoniot can be approximated [McQueen et al., 1967]

$$\left(\frac{\partial P}{\partial \rho}\right)_H = \frac{\rho_o(2K_{os} - \rho_H^2 \gamma P_H)}{\rho_H \{ \gamma P_H - (2 + \gamma) \rho_o \}} \quad (31)$$

The resulting slope obtained shows a simple increase in the slope, as seen in Fig. 4. The uncertainty of the calculated slope, however, becomes greater with increasing pressure and it may be hard to say that the initial slope of isentropic expansion is steeper than that of Hugoniot at high pressures.

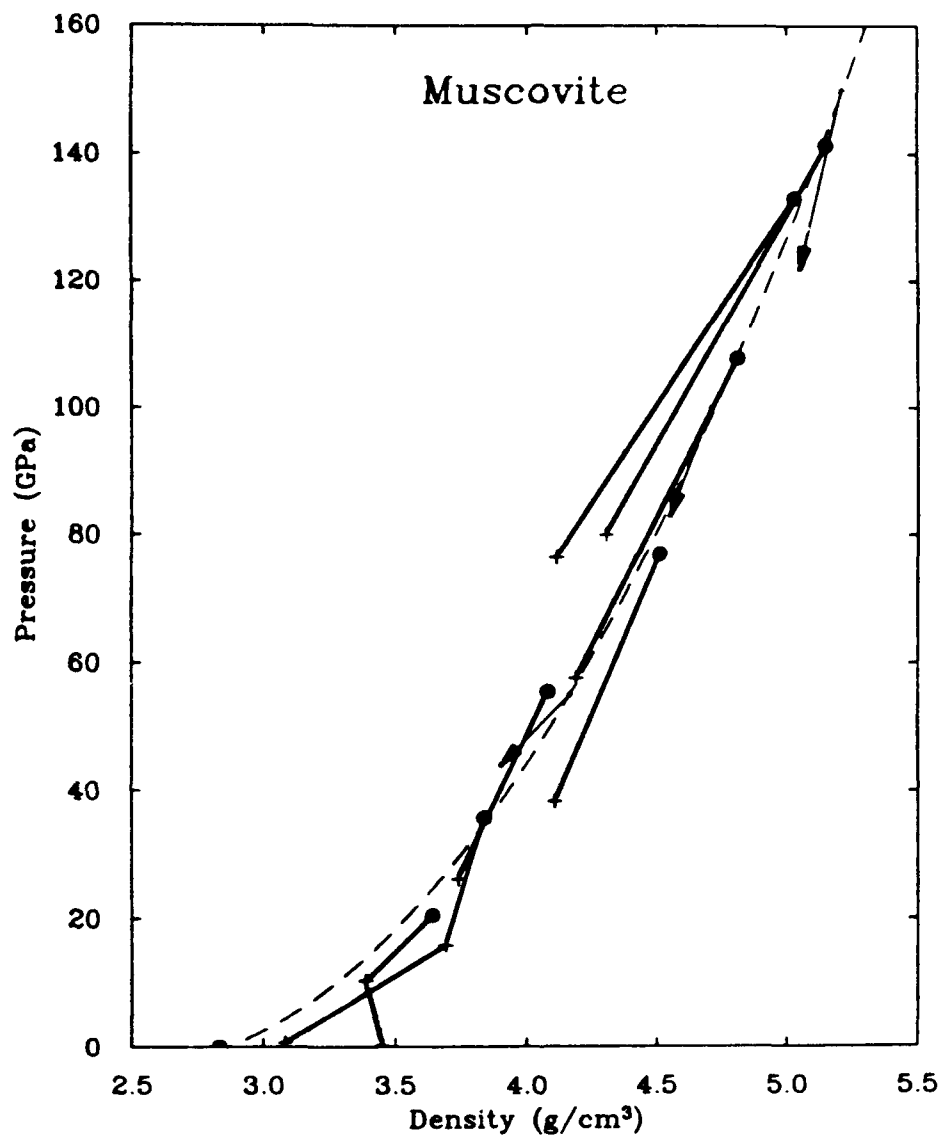


Figure 2-4. Pressure-density relations for muscovite showing adiabatic release states. Solid circles are Hugoniot states and pluses represent measured partial release states (Table 3). Solid lines serve only to connect the data sets and are not intended to represent the actual release path. Arrows indicate calculated slopes obtained from eq. (31).

Table 3. Hugoniot and Partial Release States of Muscovite (initial density : $2.835 \pm 0.002 \text{ g/cm}^3$)

Shot#	Impactor	Hugoniot State				Partial Release State				
		Velocity (km/sec)	Final shock velocity (km/sec)	Final particle velocity (km/sec)	Shock pressure (GPa)	Density (g/cm ³)	Buffer shock velocity (km/sec)	Buffer particle velocity (km/sec)	Pressure (GPa)	Density (g/cm ³)
831	Cu,	1.76 ±0.01	5.72 ±0.15	1.27 ±0.02	20.5 ±0.5	3.641 ±0.036	lexan 5.03 ±0.02 polystyrene	1.72 ±0.01	10.3 ±0.1	3.388 ±0.046
828	Ta,	2.34 ±0.01	6.94 ±0.08	1.81 ±0.01	35.7 ±0.04	3.837 ±0.020	lexan 5.84 ±0.12 polystyrene	2.26 ±0.08	15.8 ±0.9	3.692 ±0.060
224	Al,	4.83 ±0.10	8.01 ±0.08	2.44 ±0.06	55.5 ±1.4	4.080 ±0.050	3.94 ±0.09 lexan 6.72 ±0.66 lexan	3.31 ±0.08 3.26 ±0.50	0.65 ±0.04 26.1 ±6.6	3.083 ±0.069 3.738 ±0.466
226	Cu,	4.60 ±0.04	8.55 ±0.08	3.18 ±0.03	77.0 ±0.9	4.511 ±0.040	lexan 7.83 ±0.15 lexan	4.10 ±0.11	38.3 ±1.8	4.106 ±0.123
223	Cu,	5.77 ±0.03	9.62 ±0.21	3.95 ±0.03	107.8 ±1.9	4.813 ±0.093	lexan 9.29 ±0.30 lexan	5.20 ±0.23	57.6 ±4.4	4.188 ±0.259
225	Ta,	6.05 ±0.05	10.37 ±0.21	4.53 ±0.04	133.1 ±2.5	5.031 ±0.101	lexan 10.49 ±0.11 lexan	6.11 ±0.09	76.5 ±1.9	4.114 ±0.311
221	Ta,	6.33 ±0.04	10.53 ±0.15	4.74 ±0.03	141.4 ±1.9	5.153 ±0.078	lexan 10.70 ±0.35	6.27 ±0.26	80.0 ±6.0	4.304 ±0.324

According to the investigations of micas in experimentally shocked gneiss [Lambert and Mackinnon, 1984] localized melting of muscovite begins upon release from some 30 GPa and is completed at 70 GPa. Note that the shock-melting was congruent and the decomposition products of muscovite were not observed experimentally. Moreover, the final shock states in the shock-recovery experiments were achieved via multiple reverberation while those of the equation-of-state experiments were determined under a single shock compression. The final pressures in recovery experiments are those in the stainless steel containers and the initial shock pressure can be calculated as low as 10 to 15 GPa.

Phase relations of muscovite under static pressure conditions [Huang and Wyllie, 1973] indicate that muscovite decomposes into orthoclase, corundum, and vapor below about 1 GPa and 825 °C, and that it will melt incongruently above that pressure and temperature. If muscovite melts incongruently upon release from the shock compression, then the structural water in the muscovite may be expelled at considerably low pressures during the pressure release process. The pressures determined as partially released states are apparently too high to result in volatilization. When the pressure of partial release state comes down to the ~1 GPa pressure level, we expect shallow release paths and much lower densities. This behavior is observed in the case of brucite [Duffy et al., 1991].

Conclusions

(1) Shock equation of state data of muscovite are determined between 20 and 140 GPa, and can be fit by a linear U_s - U_p relation:

$$U_s = 4.62 + 1.27 U_p \text{ (km/sec).}$$

(2) Muscovite apparently remains stable along its Hugoniot. Third order Birch-Murnaghan equation of state parameters are: $K_{OS} = 52 \pm 4$ GPa and $K'_{OS} = 3.2 \pm 0.3$. These parameters are comparable with the other hydrous minerals such as brucite, serpentine, and tremolite, although the water content varies from 2 to 30 wt % among these minerals.

parameters are comparable with the other hydrous minerals such as brucite, serpentine, and tremolite, although the water content varies from 2 to 30 wt % among these minerals.

(3) Thermodynamic and theoretical calculations, however, suggest that muscovite dehydrates into the hollandite KAlSi_3O_8 , Al_2O_3 , and H_2O with only a small volume change above a pressure near 70 GPa.

(4) Observed release paths indicate a change of the slope in the density-pressure plane near 80 GPa, suggesting vaporization upon adiabatic pressure release.

Acknowledgments

We are grateful to Dr. C. A. Francis, Curator, Harvard Mineral Collection for providing the high quality muscovite sample. Michael Long and Epaproditto Gelle maintained the guns and prepared the samples. John Beckett helped us to make granite glass for probe analysis.

REFERENCES

- Ahrens, T. J., Shock wave techniques for geophysics and planetary physics, in *Methods of Experimental Physics*, vol. 24, Part A, edited by C. G. Sammis and T. L. Henyey, pp. 185-235, Academic Press, New York, 1987.
- Ahrens, T. J., D. L. Anderson, and A. E. Ringwood, Equation of state and crystal structures of high-pressure phases of shocked silicates and oxides, *Rev. Geophys.*, **7**, 667-707, 1969.
- Ahrens, T. J., and R. Jeanloz, Pyrite: Shock compression, isentropic release, and composition of the Earth's core, *J. Geophys. Res.*, **92**, 10363-75, 1987.
- Ahrens, T. J., and H.-P. Liu, A shock-induced phase change in orthoclase, *J. Geophys. Res.*, **78**, 1274-1278, 1973.
- Ahrens, T. J., C. F. Peterson, and J. T. Rosenberg, Shock compression of feldspars, *J. Geophys. Res.*, **74**, 2727-2746, 1969.
- Ahrens, T. J., and J. T. Rosenberg, *Shock metamorphism: Experiments on quartz and plagioclase*, Mono Book Corp., Baltimore, 1-59-81, 1968.
- Al'tshuler, L. V., and I. I. Sharipdzhanov, Additive equations of state of silicates at high pressures, *Izv. Earth Phys.*, **3**, 11-28, 1971.
- Angel, R. J., R. M. Hazen, T. C. McCormick, C. T. Prewitt, and J. R. Smyth, Comparative compressibility of end-member feldspars, *Phys. Chem. Minerals*, **15**, 313-318, 1988.
- Barker, L. M., and R. E. Hollenbach, Laser interferometer for measuring high velocities of any reflecting surface, *J. Appl. Phys.*, **43**, 4669-4675, 1972.
- Boslough, M., Postshock temperatures in silica, *J. Geophys. Res.*, **93**, 6477-6484, 1988.
- Boslough, M. B., T. J. Ahrens, and A. C. Mitchell, Shock temperatures in anorthite glass, *Geophys. J.R. Astr. Soc.*, **84**, 475-489, 1986.
- Bridgman, P. W., Linear compressions to 30,000 Kg/cm², including relatively incompressible substances, *Proc. Am. Acad. Arts Sci.*, **77**, 189-234, 1949.
- Brown, J. M., and J. W. Shaner, Rarefaction velocities in shocked tantalum and the high pressure melting point, in *Shock Waves in Condensed Matter-1983*, edited by J. R. Asay, R. A. Graham and G. K. Straub, pp. 91-94, Elsevier, New York, 1984.
- Chatterjee, N. D., and W. Johannes, Thermal stability and standard thermodynamic properties of synthetic 2M-muscovite, KAl₂[AlSi₃O₁₀(OH)₂], *Contr. Mineral. Petrol.*, **48**, 89-114, 1974.
- Chhabildas, L. C., and D. E. Grady, Dynamic material response of quartz at high strain rates, in *Mat. Res. Soc. Symp. Proc.*, vol. 22, pp. 147-150, 1984.
- Chhabildas, L. C., and J. M. Miller, Release-adiabat measurements in crystalline quartz, Sandia National Laboratory, Albuquerque, SAND 85-1092, 25 pp., 1985.
- Cummings, D., Shock deformation of biotite around a nuclear explosion, in *Shock Metamorphism of Natural Materials*, edited by B. M. French and N. M. Short, pp. 211-218, Mono Book Corp., Baltimore, 1968.
- DeCarli, P. S., and J. C. Jamieson, Formation of an amorphous form of quartz under shock conditions, *J. Chem. Phys.*, **31**, 1675-1676, 1959.
- Duffy, T. S., T. J. Ahrens, and M. A. Lange, The equation of state of brucite Mg(OH)₂, *J. Geophys. Res.*, *in press*, 1991.
- Eugster, H. P., A. L. Albee, A. E. Bence, and J. B. Thompson Jr., The two-phase region and excess mixing properties of paragonite-muscovite crystalline solutions, *J. Petrol.*, **13**, 147-179, 1972.
- Grady, D. E., W. I. Murri, and P. S. DeCarli, Hugoniot sound velocities and phase transformation in two silicates, *J. Geophys. Res.*, **80**, 4857-4861, 1975.
- Grady, D. E., and W. J. Murri, Dynamic unloading in shock compressed feldspar, *Geophys. Res. Lett.*, 472-474, 1976.

- Grady, D. E., W. J. Murri, and G. R. Fowles, Quartz to stishovite: Wave propagation in the mixed phase region, *J. Geophys. Res.*, 332-338, 1974.
- Guggenheim, S., Y. Chang, and A. F. Koster van Groos, Muscovite dehydroxylation: High-temperature studies, *Am. Mineral.*, 72, 537-550, 1986.
- Halbach, H., and N. D. Chatterjee, An empirical Redlich-Kwong-type equation of state for water to 1000°C and 200Kbar, *Contr. Mineral. Petrol.*, 79, 337-345, 1982.
- Heinz, D. L., and R. Jeanloz, The equation of state of the gold calibration standard, *J. Appl. Phys.*, 55, 885-893, 1984.
- Hemley, R. J., A. P. Jephcoat, H. K. Mao, M. C. Ming, and M. H. Manghnani, Pressure induced amorphization of crystalline silica, *Nature*, 334, 52, 1988.
- Hemling, W., Velocity sensing interferometer (VISAR) modification, *Rev. Sci. Instrum.*, 50, 73-78, 1979.
- Heyman, D., and F. Hörz, Raman spectroscopy and x-ray diffractometer studies of experimentally produced diaplectic feldspar glass, *Phys. Chem. Mineral.*, 17, 38-44, 1990.
- Hörz, F., and T. J. Ahrens, Deformation of experimentally shocked biotite, *Am. J. Sci.*, 267, 1213-1299, 1969.
- Huang, W. L., and P. J. Wyllie, Muscovite dehydration and melting in deep crust and subducted oceanic sediments, *Earth Planet. Sci. Lett.*, 18, 133-136, 1973.
- Hurlbut, C. S., Jr., Muscovite from Methuen Township, Ontario, *Am. Mineral.*, 41, 892-898, 1956.
- Jackson, I., and T. J. Ahrens, Shock-wave compression of single crystal forsterite, *J. Geophys. Res.*, 84, 3039-3048, 1979.
- Jeanloz, R., Shock wave equation of state and finite strain theory, *J. Geophys. Res.*, 94, 5873-5886, 1989.
- Jeanloz, R., and T. J. Ahrens, Pyroxenes and olivines: Structural implications of shock-wave data for high pressure phases, in *High-Pressure Research: Applications to Geophysics*, edited by M. H. Manghnani and S. Akimoto, pp. 439-462, Academic Press, New York, 1977.
- Kinomura, N., S. Kume, and M. Koizumi, Synthesis of $K_2SiSi_3O_4$ with silicon in 4- and 6-coordination, *Mineral. Mag.*, 40, 401-404, 1975.
- Kleeman, J. D., Formation of diaplectic glass by experimental shock loading of orthoclase, *J. Geophys. Res.*, 76, 5499-5503, 1971.
- Lambert, P., and I. D. R. Mackinnon, Micas in experimentally shocked gneiss, *Proc. 14th Lunar Planet. Sci. Conf., J. Geophys. Res.*, 89, B685-B699, 1984.
- Liu, L., and W. A. Bassett, *Elements, Oxides, and Silicates: High-Pressure Phases with Implications for the Earth's Interior*, Oxford Univ. Press., New York, 1986.
- Lyzenga, G. A., and T. J. Ahrens, The relation between the shock-induced free surface velocity and the post-shock specific volume of solids, *J. Appl. Phys.*, 49, 201-204, 1978.
- Lyzenga, G. A., T. J. Ahrens, and A. C. Mitchell, Shock temperatures of SiO_2 and their geophysical implications, *J. Geophys. Res.*, 88, 2431-2444, 1983.
- Marsh, S. P. (Ed.), *LASL Shock Hugoniot Data*, pp. 1-327, University of California Press, Berkeley, CA, 1980.
- McQueen, R. G., J. N. Fritz, and S. P. Marsh, On the equation of state of stishovite, *J. Geophys. Res.*, 68, 2319, 1963.
- McQueen, R. G., S. P. Marsh, J. W. Taylor, J. N. Fritz, and W. J. Crater, The equation of state of solids from shock wave studies, in *High-Velocity Impact Phenomena*, edited by R. Kinslow, pp. 249-419, Academic Press, San Diego, 1970.
- McQueen, R. J., S. P. Marsh, and J. N. Fritz, Hugoniot equation of state of twelve rocks, *J. Geophys. Res.*, 72, 4999-5036, 1967.

- Meade, C., and R. Jeanloz, Static compression of $\text{Ca}(\text{OH})_2$ at room temperature: Observations of amorphization and equation of state measurements to 10.7 GPa, *Geophys. Res. Lett.*, **17**, 1157-1160, 1990.
- Milton, D. J., and P. S. DeCarli, Maskelynite: Formation by explosive shock, *Science*, **140**, 670-671, 1963.
- Mitchell, A. C., and W. J. Nellis, Equation of state and electrical conductivity of water and ammonia shocked to the 100 GPa (1 Mbar) pressure range, *J. Chem. Phys.*, **76**, 6273-6281, 1982.
- Nur, A., and G. Simmons, The effect of viscosity of a fluid phase on velocity in low porosity rocks, *Earth Planet. Sci. Lett.*, **7**, 99-108, 1969.
- Podurets, M. A., G. V. Simakov, and R. F. Trunin, On the phase equilibrium in shock-compressed quartz and the kinetics of phase transitions, *Physics of the Solid Earth*, **12**, 419-424, 1976.
- Raikes, S. A., and T. J. Ahrens, Post-shock temperatures of minerals, *Geophys. J. Roy. Astron. Soc.*, **58**, 717-748, 1979.
- Rice, M. H., R. G. McQueen, and J. M. Walsh, Compression of solids by strong shock waves, *Solid State Phys.*, **6**, 1-63, 1958.
- Robie, R. A., B. S. Hemingway, and J. R. Fisher, Thermodynamic properties of minerals and related substances at 298.15 K and 1 bar (10^5 Pascals) pressure and at higher temperatures, U.S. Geological Survey, Washington, U.S.G.S. Bull. No. 1452, 1978.
- Schmitt, D. R., and T. J. Ahrens, Temperatures of shock-induced shear instabilities and their relationship to fusion curves, *Geophys. Res. Lett.*, **10**, 1077-1080, 1983.
- Seki, Y., and G. C. Kennedy, The breakdown of potassium feldspar KAlSi_3O_8 at high temperatures and high pressures, *Am. Mineral.*, **49**, 1688-1706, 1964.
- Sekine, T., and T. J. Ahrens, Shock-induced transformation in the system $\text{NaAlSiO}_4\text{-SiO}_2$, to be submitted to *Phys. Chem. Minerals*, 1991.
- Sekine, T., A. Rubin, and T. J. Ahrens, Shock wave equation of state of muscovite, *J. Geophys. Res.*, to be submitted, 1991a.
- Sekine, T., A. M. Rubin, T. S. Duffy, and T. J. Ahrens, Shock compression and isentropic release of granite, *Geophys. J. R. Astr. Soc.*, present study, 1991b.
- Short, N. M., Experimental microdeformation of rock materials by shock pressures from laboratory-scale impacts and explosions, in *Shock Metamorphism of Natural Materials*, edited by B. M. French and N. M. Short, Mono Book Corp., Baltimore, 1968a.
- Short, N. M., Nuclear-explosion-induced microdeformation of rocks: An aid to the recognition of meteorite impact structures, in *Shock Metamorphism of Natural Materials*, edited by B. M. French and N. M. Short, pp. 185-210, Mono Press, Baltimore, 1968b.
- Simakov, G. V., N. M. Pavlovsky, N. G. Kalashnikov, and R. F. Trunin, Shock compressibility of twelve minerals, *Izv. Phys. Solid Earth*, **10**, 11-17, 1974.
- Simakov, G. V., and R. F. Trunin, The compression of minerals by shock waves, *Izv. Earth Physics*, **16**, 134-137, 1980.
- Stöffler, D., and U. Hornemann, Quartz and feldspar glasses produced by natural and experimental shock, *Meteoritics*, **7**, 371-394, 1972.
- Swegle, J. W., Irreversible phase transitions and wave propagation in silicate geologic materials, Sandia, SAND 89-1443, 1989.
- Swegle, J. W., Irreversible phase transition and wave propagation in silicate materials, *J. Appl. Phys.*, **68**, 1563-1579, 1990.
- Tan, H., and T. J. Ahrens, Shock-induced polymorphic transition in quartz, carbon, and boron nitride, *J. Appl. Phys.*, **67**, 217-224, 1990.

- Tattevin, H., Y. Syono, M. Kikuchi, K. Kusaba, and B. Velde, Shock deformation of alpha quartz: Laboratory experiments and TEM investigation, *Eur. J. Mineral.*, 2, 227-234, 1990.
- Telegin, G. S., V. G. Antoshev, V. A. Bugayeva, G. V. Simakov, and R. F. Trunin, Calculated determination of Hugoniot curves of rocks and minerals, *Izv. Earth Phys.*, 16, 319-324, 1980.
- Trunin, R. F., Compressibility of various substances at high shock pressures: An overview, *Izvest. Earth Phys.*, 22, 103-114, 1986.
- Trunin, R. F., G. V. Simakov, I. P. Dudoladov, G. S. Telegin, and I. P. Trusov, Rock compressibility in shock waves, *Izv., Earth Physics*, 24, 38-42, 1988.
- Trunin, R. F., G. V. Simakov, M. A. Podurets, B. N. Moiseyev, and L. V. Popov, Dynamic compressibility of quartz and quartzite at high pressure, *Izv. Earth Phys.*, 1, 3-12, 1970.
- Tyburczy, J. A., T. S. Duffy, and T. J. Ahrens, Shock wave equation of state of serpentine to 150 GPa: Implications of the occurrence of water in the Earth's lower mantle, *J. Geophys. Res.*, submitted, 1990.
- Van Thiel, M., Compendium of Shock Wave Data, Lawrence Livermore Laboratory, Livermore, UCRL-50108, 1977.
- Vaughan, M. T., and S. Guggenheim, Elasticity of muscovite and its relationship to crystal structure, *J. Geophys. Res.*, 91, 4657-4664, 1986.
- Velde, B., Y. Syono, M. Kikuchi, and H. Boyer, Raman microprobe study of synthetic diaplectic plagioclase feldspars, *Phys. Chem. Mineral*, 16, 436-441, 1989.
- Wackerle, J., Shock-wave compression of quartz, *J. Appl. Phys.*, 33, 922-937, 1962.
- Williams, Q., and R. Jeanloz, Static amorphization of anorthite at 300K and comparison with diaplectic glass, *Nature*, 338, 413-415, 1989.
- Williams, Q., E. Knittle, R. Reichlin, S. Martin, and R. Jeanloz, Structural and electrical properties of Fe_2SiO_4 - fayalite at ultrahigh pressures: Amorphization and gap closure, *J. Geophys. Res.*, 95, 21549-21563, 1990.

Prof. Thomas Ahrens
Seismological Lab, 252-21
Division of Geological & Planetary Sciences
California Institute of Technology
Pasadena, CA 91125

Prof. Charles B. Archambeau
CIRES
University of Colorado
Boulder, CO 80309

Dr. Thomas C. Bache, Jr.
Science Applications Int'l Corp.
10260 Campus Point Drive
San Diego, CA 92121 (2 copies)

Prof. Muawia Barazangi
Institute for the Study of the Continent
Cornell University
Ithaca, NY 14853

Dr. Jeff Barker
Department of Geological Sciences
State University of New York
at Binghamton
Vestal, NY 13901

Dr. Douglas R. Baumgardt
ENSCO, Inc
5400 Port Royal Road
Springfield, VA 22151-2388

Prof. Jonathan Berger
IGPP, A-025
Scripps Institution of Oceanography
University of California, San Diego
La Jolla, CA 92093

Dr. Gilbert A. Bollinger
Department of Geological Sciences
Virginia Polytechnical Institute
21044 Derring Hall
Blacksburg, VA 24061

Dr. Lawrence J. Burdick
Woodward-Clyde Consultants
566 El Dorado Street
Pasadena, CA 91109-3245

Dr. Jerry Carter
Center for Seismic Studies
1300 North 17th St., Suite 1450
Arlington, VA 22209-2308

Prof. Vernon F. Cormier
Department of Geology & Geophysics
U-45, Room 207
The University of Connecticut
Storrs, CT 06268

Professor Anton W. Dainty
Earth Resources Laboratory
Massachusetts Institute of Technology
42 Carleton Street
Cambridge, MA 02142

Prof. Steven Day
Department of Geological Sciences
San Diego State University
San Diego, CA 92182

Dr. Zoltan A. Der
ENSCO, Inc.
5400 Port Royal Road
Springfield, VA 22151-2388

Prof. Lewis M. Duncan
Dept. of Physics & Astronautics
Clemson University
Clemson, SC 29634-1901

Prof. John Ferguson
Center for Lithospheric Studies
The University of Texas at Dallas
P.O. Box 830688
Richardson, TX 75083-0688

Dr. Mark D. Fisk
Mission Research Corporation
735 State Street
P. O. Drawer 719
Santa Barbara, CA 93102

Prof. Stanley Flatte
Applied Sciences Building
University of California
Santa Cruz, CA 95064

Dr. Alexander Florence
SRI International
333 Ravenswood Avenue
Menlo Park, CA 94025-3493

Dr. Clifford Frohlich
Institute of Geophysics
8701 North Mopac
Austin, TX 78759

Dr. Holy K. Given
IGPP, A-025
Scripps Institute of Oceanography
University of California, San Diego
La Jolla, CA 92093

Prof. Henry L. Gray
Vice Provost and Dean
Department of Statistical Sciences
Southern Methodist University
Dallas, TX 75275

Dr. Indra Gupta
Teledyne Geotech
314 Montgomery Street
Alexandria, VA 22314

Prof. David G. Harkrider
Seismological Laboratory
Division of Geological & Planetary Sciences
California Institute of Technology
Pasadena, CA 91125

Prof. Danny Harvey
CIRES
University of Colorado
Boulder, CO 80309

Prof. Donald V. Helmberger
Seismological Laboratory
Division of Geological & Planetary Sciences
California Institute of Technology
Pasadena, CA 91125

Prof. Eugene Herrin
Institute for the Study of Earth and Man
Geophysical Laboratory
Southern Methodist University
Dallas, TX 75275

Prof. Bryan Isacks
Cornell University
Department of Geological Sciences
SNEE Hall
Ithaca, NY 14850

Dr. Rong-Song Jih
Teledyne Geotech
314 Montgomery Street
Alexandria, VA 22314

Prof. Lane R. Johnson
Seismographic Station
University of California
Berkeley, CA 94720

Dr. Richard LaCoss
MIT-Lincoln Laboratory
M-200B
P. O. Box 73
Lexington, MA 02173-0073 (3 copies)

Prof Fred K. Lamb
University of Illinois at Urbana-Champaign
Department of Physics
1110 West Green Street
Urbana, IL 61801

Prof. Charles A. Langston
Geosciences Department
403 Deike Building
The Pennsylvania State University
University Park, PA 16802

Prof. Thorne Lay
Institute of Tectonics
Earth Science Board
University of California, Santa Cruz
Santa Cruz, CA 95064

Prof. Arthur Lerner-Lam
Lamont-Doherty Geological Observatory
of Columbia University
Palisades, NY 10964

Dr. Christopher Lynnes
Teledyne Geotech
314 Montgomery Street
Alexandria, VA 22314

Prof. Peter Malin
Department of Geology
Old Chemistry Bldg.
Duke University
Durham, NC 27706

Dr. Randolph Martin, III
New England Research, Inc.
76 Olcott Drive
White River Junction, VT 05001

Prof. Thomas V. McEvelly
Seismographic Station
University of California
Berkeley, CA 94720

Dr. Keith L. McLaughlin
S-CUBED
A Division of Maxwell Laboratory
P.O. Box 1620
La Jolla, CA 92038-1620

Prof. William Menke
Lamont-Doherty Geological Observatory
of Columbia University
Palisades, NY 10964

Stephen Miller
SRI International
333 Ravenswood Avenue
Box AF 116
Menlo Park, CA 94025-3493

Prof. Bernard Minster
IGPP, A-025
Scripps Institute of Oceanography
University of California, San Diego
La Jolla, CA 92093

Prof. Brian J. Mitchell
Department of Earth & Atmospheric Sciences
St. Louis University
St. Louis, MO 63156

Mr. Jack Murphy
S-CUBED, A Division of Maxwell Laboratory
11800 Sunrise Valley Drive
Suite 1212
Reston, VA 22091 (2 copies)

Prof. John A. Orcutt
IGPP, A-025
Scripps Institute of Oceanography
University of California, San Diego
La Jolla, CA 92093

Prof. Keith Priestley
University of Cambridge
Bullard Labs, Dept. of Earth Sciences
Madingley Rise, Madingley Rd.
Cambridge CB3 0EZ, ENGLAND

Dr. Jay J. Pulli
Radix Systems, Inc.
2 Taft Court, Suite 203
Rockville, MD 20850

Prof. Paul G. Richards
Lamont Doherty Geological Observatory
of Columbia University
Palisades, NY 10964

Dr. Wilmer Rivers
Teledyne Geotech
314 Montgomery Street
Alexandria, VA 22314

Prof. Charles G. Sammis
Center for Earth Sciences
University of Southern California
University Park
Los Angeles, CA 90089-0741

Prof. Christopher H. Scholz
Lamont-Doherty Geological Observatory
of Columbia University
Palisades, NY 10964

Thomas J. Sereno, Jr.
Science Application Int'l Corp.
10260 Campus Point Drive
San Diego, CA 92121

Prof. David G. Simpson
Lamont-Doherty Geological Observatory
of Columbia University
Palisades, NY 10964

Dr. Jeffrey Stevens
S-CUBED
A Division of Maxwell Laboratory
P.O. Box 1620
La Jolla, CA 92038-1620

Prof. Brian Stump
Institute for the Study of Earth & Man
Geophysical Laboratory
Southern Methodist University
Dallas, TX 75275

Prof. Jeremiah Sullivan
University of Illinois at Urbana-Champaign
Department of Physics
1110 West Green Street
Urbana, IL 61801

Prof. Clifford Thurber
University of Wisconsin-Madison
Department of Geology & Geophysics
1215 West Dayton Street
Madison, WI 53706

Prof. M. Nafi Toksoz
Earth Resources Lab
Massachusetts Institute of Technology
42 Carleton Street
Cambridge, MA 02142

Prof. John E. Vidale
University of California at Santa Cruz
Seismological Laboratory
Santa Cruz, CA 95064

Prof. Terry C. Wallace
Department of Geosciences
Building #77
University of Arizona
Tucson, AZ 85721

Dr. William Wortman
Mission Research Corporation
8560 Cinderbed Rd.
Suite # 700
Newington, VA 22122

Prof. Francis T. Wu
Department of Geological Sciences
State University of New York
at Binghamton
Vestal, NY 13901

Prof. John Ebel
Department of Geology & Geophysics
Boston College
Chestnut Hill, MA 02167

Eric Fielding
SNEE Hall
INSTOC
Cornell University
Ithaca, NY 14853

Dr. John Foley
Phillips Laboratory/LWH
Hanscom AFB, MA 01731-5000

Prof. Donald Forsyth
Department of Geological Sciences
Brown University
Providence, RI 02912

Dr. Cliff Frolich
Institute of Geophysics
8701 North Mopac
Austin, TX 78759

Dr. Anthony Gangi
Texas A&M University
Department of Geophysics
College Station, TX 77843

Dr. Freeman Gilbert
IGPP, A-025
Scripps Institute of Oceanography
University of California
La Jolla, CA 92093

Mr. Edward Giller
Pacific Sierra Research Corp.
1401 Wilson Boulevard
Arlington, VA 22209

Dr. Jeffrey W. Given
SAIC
10260 Campus Point Drive
San Diego, CA 92121

Prof. Stephen Grand
University of Texas at Austin
Department of Geological Sciences
Austin, TX 78713-7909

Prof. Roy Greenfield
Geosciences Department
403 Deike Building
The Pennsylvania State University
University Park, PA 16802

Dan N. Hagedorn
Batelle
Pacific Northwest Laboratories
Batelle Boulevard
Richland, WA 99352

Dr. James Hannon
Lawrence Livermore National Laboratory
P. O. Box 808
Livermore, CA 94550

Prof. Robert B. Herrmann
Dept. of Earth & Atmospheric Sciences
St. Louis University
St. Louis, MO 63156

Ms. Heidi Houston
Seismological Laboratory
University of California
Santa Cruz, CA 95064

Kevin Hutchenson
Department of Earth Sciences
St. Louis University
3507 Laclede
St. Louis, MO 63103

Dr. Hans Israelsson
Center for Seismic Studies
1300 N. 17th Street, Suite 1450
Arlington, VA 22209-2308

Prof. Thomas H. Jordan
Department of Earth, Atmospheric
and Planetary Sciences
Massachusetts Institute of Technology
Cambridge, MA 02139

Prof. Alan Kafka
Department of Geology & Geophysics
Boston College
Chestnut Hill, MA 02167

Robert C. Kemerait
ENSCO, Inc.
445 Pineda Court
Melbourne, FL 32940

Dr. Susan Schwartz
Institute of Tectonics
1156 High St.
Santa Cruz, CA 95064

John Sherwin
Teledyne Geotech
3401 Shiloh Road
Garland, TX 75041

Dr. Matthew Sibol
Virginia Tech
Seismological Observatory
4044 Derring Hall
Blacksburg, VA 24061-0420

Dr. Albert Smith
Lawrence Livermore National Laboratory
L-205
P. O. Box 808
Livermore, CA 94550

Prof. Robert Smith
Department of Geophysics
University of Utah
1400 East 2nd South
Salt Lake City, UT 84112

Dr. Stewart W. Smith
Geophysics AK-50
University of Washington
Seattle, WA 98195

Donald L. Springer
Lawrence Livermore National Laboratory
L-205
P. O. Box 808
Livermore, CA 94550

Dr. George Sutton
Rondout Associates
P.O. Box 224
Stone Ridge, NY 12484

Prof. L. Sykes
Lamont-Doherty Geological Observatory
of Columbia University
Palisades, NY 10964

Prof. Pradeep Talwani
Department of Geological Sciences
University of South Carolina
Columbia, SC 29208

Dr. David Taylor
ENSCO, Inc.
445 Pineda Court
Melbourne, FL 32940

Dr. Steven R. Taylor
Lawrence Livermore National Laboratory
L-205
P. O. Box 808
Livermore, CA 94550

Professor Ta-Liang Teng
Center for Earth Sciences
University of Southern California
University Park
Los Angeles, CA 90089-0741

Dr. Gregory van der Vink
IRIS, Inc.
1616 North Fort Myer Drive
Suite 1440
Arlington, VA 22209

Professor Daniel Walker
University of Hawaii
Institute of Geophysics
Honolulu, HI 96822

William R. Walter
Seismological Laboratory
University of Nevada
Reno, NV 89557

Dr. Raymond Willeman
Phillips Laboratory/LWH
Hanscom AFB, MA 01731-5000

Dr. Gregory Wojcik
Weidlinger Associates
4410 El Camino Real
Suite 110
Los Altos, CA 94022

Dr. Lorraine Wolf
Phillips Laboratory/LWH
Hanscom AFB, MA 01731-5000

Dr. Gregory B. Young
ENSCO, Inc.
5400 Port Royal Road
Springfield, VA 22151-2388

Dr. Eileen Vergino
Lawrence Livermore National Laboratory
L-205
P. O. Box 808
Livermore, CA 94550

J. J. Zucca
Lawrence Livermore National Laboratory
P. O. Box 808
Livermore, CA 94550

GOVERNMENT

Dr. Ralph Alewine III
DARPA/NMRO
1400 Wilson Boulevard
Arlington, VA 22209-2308

Dr. Dale Glover
DIA/DT-1B
Washington, DC 20301

Mr. James C. Battis
Phillips Laboratory/LWH
Hanscom AFB, MA 01731-5000

Dr. T. Hanks
USGS
Nat'l Earthquake Research Center
345 Middlefield Road
Menlo Park, CA 94025

Harley Benz
U.S. Geological Survey, MS-977
345 Middlefield Rd.
Menlo Park, CA 94025

Dr. Roger Hansen
AFTAC/TT
Patrick AFB, FL 32925

Dr. Robert Blandford
AFTAC/TT
Center for Seismic Studies
1300 North 17th St. Suite 1450
Arlington, VA 22209-2308

Paul Johnson
ESS-4, Mail Stop J979
Los Alamos National Laboratory
Los Alamos, NM 87545

Eric Chael
Division 9241
Sandia Laboratory
Albuquerque, NM 87185

Janet Johnston
Phillips Laboratory/LWH
Hanscom AFB, MA 01731-5000

Dr. John J. Cipar
Phillips Laboratory/LWH
Hanscom AFB, MA 01731-5000

Dr. Katharine Kadinsky-Cade
Phillips Laboratory/LWH
Hanscom AFB, MA 01731-5000

Cecil Davis
Group P-15, Mail Stop D406
P.O. Box 1663
Los Alamos National Laboratory
Los Alamos, NM 87544

Ms. Ann Kerr
IGPP, A-025
Scripps Institute of Oceanography
University of California, San Diego
La Jolla, CA 92093

Mr. Jeff Duncan
Office of Congressman Markey
2133 Rayburn House Bldg.
Washington, DC 20515

Dr. Max Koontz
US Dept of Energy/DP 5
Forrestal Building
1000 Independence Avenue
Washington, DC 20585

Dr. Jack Evernden
USGS - Earthquake Studies
345 Middlefield Road
Menlo Park, CA 94025

Dr. W.H.K. Lee
Office of Earthquakes, Volcanoes,
& Engineering
345 Middlefield Road
Menlo Park, CA 94025

Art Frankel
USGS
922 National Center
Reston, VA 22092

Dr. William Leith
U.S. Geological Survey
Mail Stop 928
Reston, VA 22092

Dr. Richard Lewis
Director, Earthquake Engineering & Geophysics
U.S. Army Corps of Engineers
Box 631
Vicksburg, MS 39180

James F. Lewkowicz
Phillips Laboratory/LWH
Hanscom AFB, MA 01731-5000

Mr. Alfred Lieberman
ACDA/VI-OA'State Department Bldg
Room 5726
320 - 21st Street, NW
Washington, DC 20451

Stephen Mangino
Phillips Laboratory/LWH
Hanscom AFB, MA 01731-5000

Dr. Robert Masse
Box 25046, Mail Stop 967
Denver Federal Center
Denver, CO 80225

Art McGarr
U.S. Geological Survey, MS-977
345 Middlefield Road
Menlo Park, CA 94025

Richard Morrow
ACDA/VI, Room 5741
320 21st Street N.W
Washington, DC 20451

Dr. Carl Newton
Los Alamos National Laboratory
P.O. Box 1663
Mail Stop C335, Group ESS-3
Los Alamos, NM 87545

Dr. Bao Nguyen
AFTAC/TTR
Patrick AFB, FL 32925

Dr. Kenneth H. Olsen
Los Alamos Scientific Laboratory
P. O. Box 1663
Mail Stop D-406
Los Alamos, NM 87545

Mr. Chris Paine
Office of Senator Kennedy
SR 315
United States Senate
Washington, DC 20510

Colonel Jerry J. Perrizo
AFOSR/NP, Building 410
Bolling AFB
Washington, DC 20332-6448

Dr. Frank F. Pilotte
HQ AFTAC/TT
Patrick AFB, FL 32925-6001

Katie Poley
CIA-ACIS/TMC
Room 4X16NHB
Washington, DC 20505

Mr. Jack Rachlin
U.S. Geological Survey
Geology, Rm 3 C136
Mail Stop 928 National Center
Reston, VA 22092

Dr. Robert Reinke
WL/NTESG
Kirtland AFB, NM 87117-6008

Dr. Byron Ristvet
HQ DNA, Nevada Operations Office
Attn: NVCG
P.O. Box 98539
Las Vegas, NV 89193

Dr. George Rothe
HQ AFTAC/TTR
Patrick AFB, FL 32925-6001

Dr. Alan S. Ryall, Jr.
DARPA/NMRO
1400 Wilson Boulevard
Arlington, VA 22209-2308

Dr. Michael Shore
Defense Nuclear Agency/SPSS
6801 Telegraph Road
Alexandria, VA 22310

Mr. Charles L. Taylor
Phillips Laboratory/LWH
Hanscom AFB, MA 01731-5000

Phillips Laboratory
Attn: XO
Hanscom AFB, MA 01731-5000

Dr. Larry Turnbull
CIA-OSWR/NED
Washington, DC 20505

Phillips Laboratory
Attn: LW
Hanscom AFB, MA 01731-5000

Dr. Thomas Weaver
Los Alamos National Laboratory
P.O. Box 1663, Mail Stop C335
Los Alamos, NM 87545

DARPA/PM
1400 Wilson Boulevard
Arlington, VA 22209

Phillips Laboratory
Research Library
ATTN: SULL
Hanscom AFB, MA 01731-5000

Defense Technical Information Center
Cameron Station
Alexandria, VA 22314 (2 copies)

Phillips Laboratory
ATTN: SUL
Kirtland AFB, NM 87117-6008 (2 copies)

Defense Intelligence Agency
Directorate for Scientific & Technical Intelligence
Attn: DT1B
Washington, DC 20340-6158

Secretary of the Air Force
(SAFRD)
Washington, DC 20330

AFTAC/CA
(STINFO)
Patrick AFB, FL 32925-6001

Office of the Secretary Defense
DDR & E
Washington, DC 20330

TACTEC
Battelle Memorial Institute
505 King Avenue
Columbus, OH 43201 (Final Report Only)

HQ DNA
Attn: Technical Library
Washington, DC 20305

DARPA/RMO/RETRIEVAL
1400 Wilson Boulevard
Arlington, VA 22209

DARPA/RMO/Security Office
1400 Wilson Boulevard
Arlington, VA 22209

CONTRACTORS (FOREIGN)

Dr. Ramon Cabre, S.J.
Observatorio San Calixto
Casilla 5939
La Paz, Bolivia

Prof. Hans-Peter Harjes
Institute for Geophysik
Ruhr University/Bochum
P.O. Box 102148
4630 Bochum 1, FRG

Prof. Eystein Husebye
NTNF/NORSAR
P.O. Box 51
N-2007 Kjeller, NORWAY

Prof. Brian L.N. Kennett
Research School of Earth Sciences
Institute of Advanced Studies
G.P.O. Box 4
Canberra 2601, AUSTRALIA

Dr. Bernard Massinon
Societe Radiomana
27 rue Claude Bernard
75005 Paris, FRANCE (2 Copies)

Dr. Pierre Mecheler
Societe Radiomana
27 rue Claude Bernard
75005 Paris, FRANCE

Dr. Svein Mykkeltveit
NTNF/NORSAR
P.O. Box 51
N-2007 Kjeller, NORWAY (3 copies)

FOREIGN (OTHERS)

Dr. Peter Basham
Earth Physics Branch
Geological Survey of Canada
1 Observatory Crescent
Ottawa, Ontario, CANADA K1A 0Y3

Dr. Eduard Berg
Institute of Geophysics
University of Hawaii
Honolulu, HI 96822

Dr. Michel Bouchon
I.R.I.G.M.-B.P. 68
38402 St. Martin D'Heres
Cedex, FRANCE

Dr. Hilmar Bungum
NTNF/NORSAR
P.O. Box 51
N-2007 Kjeller, NORWAY

Dr. Michel Campillo
Observatoire de Grenoble
I.R.I.G.M.-B.P. 53
38041 Grenoble, FRANCE

Dr. Kin Yip Chun
Geophysics Division
Physics Department
University of Toronto
Ontario, CANADA M5S 1A7

Dr. Alan Douglas
Ministry of Defense
Blacknest, Brimpton
Reading RG7-4RS, UNITED KINGDOM

Dr. Manfred Henger
Federal Institute for Geosciences & Nat'l Res.
Postfach 510153
D-3000 Hanover 51, FRG

Ms. Eva Johannisson
Senior Research Officer
National Defense Research Inst.
P.O. Box 27322
S-102 54 Stockholm, SWEDEN

Dr. Fekadu Kebede
Geophysical Observatory, Science Faculty
Addis Ababa University
P. O. Box 1176
Addis Ababa, ETHIOPIA

Dr. Tormod Kvaerna
NTNF/NORSAR
P.O. Box 51
N-2007 Kjeller, NORWAY

Dr. Peter Marshall
Procurement Executive
Ministry of Defense
Blacknest, Brimpton
Reading FG7-4RS, UNITED KINGDOM

Prof. Ari Ben-Menahem
Department of Applied Mathematics
Weizman Institute of Science
Rehovot, ISRAEL 951729

Dr. Robert North
Geophysics Division
Geological Survey of Canada
1 Observatory Crescent
Ottawa, Ontario, CANADA K1A 0Y3

Dr. Frode Ringdal
NTNF/NORSAR
P.O. Box 51
N-2007 Kjeller, NORWAY

Dr. Jorg Schlittenhardt
Federal Institute for Geosciences & Nat'l Res.
Postfach 510153
D-3000 Hannover 51, FEDERAL REPUBLIC OF
GERMANY

Universita Degli Studi Di Trieste
Facolta Di Ingegneria
Istituto Di Miniere E. Geofisica Applicata, Trieste,
ITALY

Dr. John Woodhouse
Oxford University
Dept of Earth Sciences
Parks Road
Oxford OX13PR, ENGLAND